



Elastic Differential Cross Sections

Charles M. Werneth
Langley Research Center, Hampton, Virginia

Khin M. Maung and William P. Ford
University of Southern Mississippi, Hattiesburg, Mississippi

John W. Norbury
Langley Research Center, Hampton, Virginia

Michael D. Vera
University of Southern Mississippi, Hattiesburg, Mississippi

NASA STI Program . . . in Profile

Since its founding, NASA has been dedicated to the advancement of aeronautics and space science. The NASA scientific and technical information (STI) program plays a key part in helping NASA maintain this important role.

The NASA STI program operates under the auspices of the Agency Chief Information Officer. It collects, organizes, provides for archiving, and disseminates NASA's STI. The NASA STI program provides access to the NASA Aeronautics and Space Database and its public interface, the NASA Technical Report Server, thus providing one of the largest collections of aeronautical and space science STI in the world. Results are published in both non-NASA channels and by NASA in the NASA STI Report Series, which includes the following report types:

- **TECHNICAL PUBLICATION.** Reports of completed research or a major significant phase of research that present the results of NASA Programs and include extensive data or theoretical analysis. Includes compilations of significant scientific and technical data and information deemed to be of continuing reference value. NASA counterpart of peer-reviewed formal professional papers, but having less stringent limitations on manuscript length and extent of graphic presentations.
- **TECHNICAL MEMORANDUM.** Scientific and technical findings that are preliminary or of specialized interest, e.g., quick release reports, working papers, and bibliographies that contain minimal annotation. Does not contain extensive analysis.
- **CONTRACTOR REPORT.** Scientific and technical findings by NASA-sponsored contractors and grantees.
- **CONFERENCE PUBLICATION.** Collected papers from scientific and technical conferences, symposia, seminars, or other meetings sponsored or co-sponsored by NASA.
- **SPECIAL PUBLICATION.** Scientific, technical, or historical information from NASA programs, projects, and missions, often concerned with subjects having substantial public interest.
- **TECHNICAL TRANSLATION.** English-language translations of foreign scientific and technical material pertinent to NASA's mission.

Specialized services also include organizing and publishing research results, distributing specialized research announcements and feeds, providing information desk and personal search support, and enabling data exchange services.

For more information about the NASA STI program, see the following:

- Access the NASA STI program home page at <http://www.sti.nasa.gov>
- E-mail your question to help@sti.nasa.gov
- Fax your question to the NASA STI Information Desk at 443-757-5803
- Phone the NASA STI Information Desk at 443-757-5802
- Write to:
STI Information Desk
NASA Center for AeroSpace Information
7115 Standard Drive
Hanover, MD 21076-1320



Elastic Differential Cross Sections

Charles M. Werneth
Langley Research Center, Hampton, Virginia

Khin M. Maung and William P. Ford
University of Southern Mississippi, Hattiesburg, Mississippi

John W. Norbury
Langley Research Center, Hampton, Virginia

Michael D. Vera
University of Southern Mississippi, Hattiesburg, Mississippi

National Aeronautics and
Space Administration

Langley Research Center
Hampton, Virginia 23681-2199

September 2014

Acknowledgments

The authors would like to thank Drs. Steve Blattnig, Ryan Norman, Jonathan Ransom, and Francis Badavi for reviewing this manuscript. This work was supported by the Human Research Program under the Human Exploration and Operations Mission Directorate of NASA and NASA grant number NNX13AH31A. Khin Maung Maung would like to thank Alexander Maung for his helpful conversations.

Available from:

NASA Center for AeroSpace Information
7115 Standard Drive
Hanover, MD 21076-1320
443-757-5802

Contents

1	Introduction	1
2	Theory	4
2.1	Lippmann-Schwinger Equation	4
2.2	Multiple Scattering Theory	5
2.3	Matrix Element of Optical Potential	7
2.3.1	Optimum Factorization	8
2.4	Eikonal Solution Method	14
2.4.1	Nucleon-Nucleus Optical Potential	16
2.4.2	Nucleus-Nucleus Optical Potential	16
2.4.3	Optical Potential in Momentum-Space	18
2.5	Lippmann-Schwinger Partial Wave Solution Method	20
2.6	Lippmann-Schwinger 3D Solution Method	21
3	Numerical Methods	23
3.1	Eikonal	23
3.2	Partial Wave Lippmann-Schwinger	24
3.3	3D Lippmann-Schwinger	25
3.4	Localized Contributions	26
3.5	Equal Mass Kinematics	28
4	Results	30
5	Conclusions	32
6	Appendix A	32
7	Appendix B	34
8	Appendix C	35
8.1	Non-relativistic Kinematics	35
8.2	Relativistic Kinematics	36

Nomenclature

AA	Nucleus-Nucleus
CM	Center of Mass
LI	Lorentz Invariant
LS	Lippmann-Schwinger
LS3D	Three Dimensional Lippmann-Schwinger
MST	Multiple Scattering Theory
NA	Nucleon-Nucleus
NN	Nucleon-Nucleon
NR	Non-Relativistic
PW	Partial Wave
REL	Relativistic

List of Figures

1	Transition amplitude for AA scattering	40
2	Optimum factorization for AA scattering	40
3	Vectors for position space optical potential	41
4	Optical potential for low energy $p + {}^4\text{He}$ reaction	42
5	Optical potential for high energy $p + {}^4\text{He}$ reaction	42
6	Optical potential for low energy ${}^4\text{He} + {}^{20}\text{Ne}$ reaction	43
7	Optical potential for medium energy ${}^4\text{He} + {}^{20}\text{Ne}$ reaction	43
8	Optical potential for low energy ${}^4\text{He} + {}^4\text{He}$ reaction	44
9	Optical potential for high energy ${}^4\text{He} + {}^4\text{He}$ reaction	44
10	Optical potential for low energy ${}^{12}\text{C} + {}^{12}\text{C}$ reaction	45
11	Optical potential for high energy ${}^{12}\text{C} + {}^{12}\text{C}$ reaction	45
12	Kinematic functions for ${}^4\text{He} + {}^4\text{He}$ reaction	46
13	Alternate view of kinematic functions for ${}^4\text{He} + {}^4\text{He}$ reaction	46
14	Ratio of kinematic functions for ${}^4\text{He} + {}^4\text{He}$ reaction	47
15	Kinematic functions for ${}^{56}\text{Fe} + {}^{56}\text{Fe}$ reaction	47
16	Alternate view of kinematic functions for ${}^{56}\text{Fe} + {}^{56}\text{Fe}$ reaction	48
17	Ratio of kinematic functions for ${}^{56}\text{Fe} + {}^{56}\text{Fe}$ reaction	48
18	Elastic differential cross sections for $p + {}^{16}\text{O}$ reactions	49
19	Elastic differential cross sections for $p + {}^{56}\text{Fe}$ reactions	50
20	Elastic differential cross sections for ${}^4\text{He} + {}^{16}\text{O}$ reactions	51
21	Elastic differential cross sections for ${}^{12}\text{C} + {}^{56}\text{Fe}$ reactions	52
22	Elastic differential cross sections for ${}^4\text{He} + {}^4\text{He}$ reactions	53
23	Elastic differential cross sections for ${}^{20}\text{Ne} + {}^{20}\text{Ne}$ reactions	54
24	Elastic differential cross sections for ${}^{56}\text{Fe} + {}^{56}\text{Fe}$ reactions	55
25	Comparisons to experimental data	56

The eikonal, partial wave (PW) Lippmann-Schwinger, and three-dimensional Lippmann-Schwinger (LS3D) methods are compared for nuclear reactions that are relevant for space radiation applications. Numerical convergence of the eikonal method is readily achieved when exact formulas of the optical potential are used for light nuclei ($A \leq 16$) and the momentum-space optical potential is used for heavier nuclei. The PW solution method is known to be numerically unstable for systems that require a large number of partial waves, and, as a result, the LS3D method is employed. The effect of relativistic kinematics is studied with the PW and LS3D methods and is compared to eikonal results. It is recommended that the LS3D method be used for high energy nucleon-nucleus reactions and nucleus-nucleus reactions at all energies because of its rapid numerical convergence and stability.

1 Introduction

The space radiation environment is composed of solar particle emissions and ions produced from supernovae distributed throughout the galaxy [1, 2]. Solar particle events, including both coronal mass ejections and solar flares, are composed of mostly protons with energies that can exceed several hundred MeV. Galactic cosmic rays originate from the shock waves of supernovae and consist of protons and heavier ions with energies that reach hundreds of GeV per nucleon. Radiation transport codes are used to describe the transport of ions, and secondary particles produced from nuclear collisions, from the space radiation environment through shielding materials. Space radiation transport codes require cross sections for the numerous nuclear reactions that occur as a result of collisions of nuclei in the space radiation environment with nuclei in the shield. NASA’s deterministic transport code, HZETRN [3–5], currently transports all ions up to nickel—where, thereafter, incident particle fluxes are negligible [6]—with energies that extend from MeV to hundreds of GeV per nucleon through shielding materials. Efficient, accurate codes are needed for the computation of nuclear cross sections due to the large number of nuclear reactions that occur at these energies.

The Lippmann-Schwinger (LS) equation is an expression for the scattering transition amplitude [7]. Scattering amplitudes can be obtained by either solving the LS equation or by employing some approximation, such as the eikonal method. The elastic differential cross section is computed from the absolute square of the scattering amplitude, and the total cross section is related to the imaginary part of the forward scattering amplitude. The elastic cross section is obtained by performing the angular integration of the elastic differential cross section, and the reaction cross section is found from the difference between the total and elastic cross sections.

For elastic scattering, it is convenient to use the ground state and excited state projectors to write an equivalent set of coupled equations for the LS equation: the elastic

scattering equation and the defining equation for the optical potential [8, 9]. This is useful for the study of elastic scattering because all of the complications that arise from the intermediate excited states are not explicitly found in the elastic scattering equation. The input into the elastic scattering equation is the optical potential, which can be expressed in an infinite series of nucleon-nucleon (NN) transition amplitudes, t_{NN} . If the transition matrix is written for ground states of the projectile and target, then, in the factorization approximation, the first order optical potential is proportional to t_{NN} and the nuclear densities of the projectile and target [10–12]. The model of t_{NN} used in the present work is parameterized to NN total cross sections, slope parameters, and the real to imaginary ratios of the transition amplitude. Nuclear charge density distributions are obtained from electron scattering experiments [13, 14]. Matter densities of nuclei are found from nuclear charge densities by factoring out the charge distribution of the proton. The internal charge structure of the proton is not taken into account in this analysis; instead, nucleons are treated as point particles. Harmonic well densities are typically used for lighter nuclei because of the Gaussian-like decay of the nuclear charge density as a function of radial distance. Wood-Saxon densities, also known as two-parameter and three-parameter Fermi densities, are better suited for heavier nuclei, where the nuclear charge density is relatively constant before decreasing to zero at larger radial distances.

The two most common ways of solving the LS equation are to use the eikonal approximation or the method of partial wave (PW) decomposition. The eikonal approximation was first introduced by Moliere and systematically developed by Glauber in the treatment of many-body nuclear reactions with a quantum collision theory of composite objects [15]. The eikonal approximation can be derived by assuming high energy and small angle scattering, which leads to a linearized propagator in the LS equation from which the eikonal scattering wave function may be obtained [7]. The scattering amplitude is determined from the eikonal phase factor, which is a function of the optical potential [5, 16–20].

Besides being an approximation, a drawback of the eikonal approximation is that it may be numerically inefficient for the evaluation of the cross sections for a given optical potential. In the position-space representation, the optical potential, $U(\mathbf{r})$, is given by a 6-dimensional integration for heavy ion collisions [5]. Therefore, the eikonal phase factor depends on a 6-dimensional integral in the position representation of the optical potential and an additional integration variable over a coordinate in the scattering plane. The numerical integration over 7-dimensions in the position space representation is inefficient when an analytic expression of the optical potential is not known. It is desirable to use exact formulas for the optical potential when analytic expressions of the optical potential can be found. The current work implements expressions of the optical potential for nucleon-nucleus (NA) and nucleus-nucleus (AA) scattering utilizing harmonic well nuclear matter densities for light nuclei ($A \leq 16$), and the optical potential is expressed in momentum space for cases where no analytic expression can be found ($A > 16$).

The present work expresses the optical potential as a function of momentum transfer and reduces the 7-dimensional integration of the eikonal phase function to 2-dimensions,

which significantly increases numerical efficiency. An additional advantage of this formulation of the eikonal phase function is that the momentum space representation of the optical potential may be used for any nuclear density and transition amplitude, provided the Fourier transforms may be evaluated or the explicit forms of the the densities are known in momentum-space.

The LS equation may also be solved via the method of partial wave decomposition [7, 21], where the transition amplitude is expanded in an infinite series of functions of relative momenta and angular dependent spherical harmonics or Legendre polynomials. After projecting out the angular dependence, the transition amplitude is solved for a given partial wave. Once the partial wave solutions are found, the full solution for the transition amplitude is found by re-summing the series, which is terminated when some pre-defined tolerance of precision is reached.

The PW method is known to become numerically unstable for reactions that require many partial waves [7], which is not only limited to high energy NA reactions (GeV/n) but also includes AA reactions at relatively low energy per nucleon (hundreds of MeV/n). The numerical instability can be traced back to highly oscillating Legendre polynomials in the PW expansion and large on-shell momenta for elastic reactions, where contributions to the transition amplitude tend to be localized.

Although there are numerical limitations associated with the PW method, the full three-dimensional Lippmann-Schwinger (LS3D) solution method circumvents the necessity of using highly oscillating Legendre polynomials [22–26]. Most of the LS3D studies have consisted of NN interactions [22, 23, 25] with the exception of Rodriguez–Gallardo et al. [24] who studied NA and AA reactions at relatively low energies and Liu et al. [26] who studied three-body reactions. This demonstrates the validity of the method and can be compared to results generated with the PW method since few partial waves are needed for such reactions. The LS3D method is compared to the PW and eikonal methods for NA and AA reactions with energies extending from 150 MeV/n to 20 GeV/n.

The eikonal solution method is a non-relativistic approximation; however, when energies become sufficiently high, relativistic effects will be manifested in the elastic differential cross section. Relativistic kinematics are needed for high energy reactions and are easily incorporated into the momentum-space representation of the PW and LS3D equations, where the momentum is simply a number instead of a spatial derivative operator, as in the position-space representation. At relativistic energies, the PW and LS3D models will agree if convergence of the partial wave solution is reached, but both methods should differ from the eikonal results. In the low energy limit, the eikonal method should break down and begin to diverge from the PW and LS3D results because of the approximations inherent in the eikonal method. To examine the effect of kinematics, model results are compared for various nuclear reactions at relativistic and non-relativistic energies.

At relativistic energies, the inner structure of the nucleons may be probed. The multiple scattering theory (MST) upon which the model of interaction is based and the NN transition amplitude do not account for the inner structure of the nucleons. The compli-

cations associated with the inner structure of the nucleons are assumed to be included in the parameterizations to experimental NN transition amplitudes.

In this paper, exact formulas are presented for the optical potential in the position space representation for light nuclei. A momentum-space representation of the eikonal approximation is presented and used for heavier nuclei. Both methods are utilized in the present work and are significantly more efficient than performing the usual eikonal calculation in the position-space representation. The PW and LS3D methods are solved with non-relativistic and relativistic kinematics, and comparisons of the models are made for reactions that are relevant to space radiation. Additional comparisons to experimental data are presented. Based on the results presented herein, it is recommended that the LS3D method be used for high energy NA reactions and AA reactions at all energies because of its rapid numerical convergence and stability. The effect of the kinematics for projectiles and targets with equal masses and extensive comparisons to experimental data will be communicated in subsequent manuscripts.

The present work is organized as follows. In section 2, a theoretical overview of the LS equation, MST, the elastic scattering equation, and the optical potential are reviewed. This is followed by a discussion of the eikonal, PW, and LS3D methods. The numerical solution methods are discussed in section 3, and model comparisons are given in section 4. The conclusions are stated in section 5.

2 Theory

2.1 Lippmann-Schwinger Equation

The LS equation is an expression for the scattering transition operator—the fundamental quantity that is used to evaluate the elastic differential, elastic, reaction, and total cross sections for nuclear reactions—and is given as

$$T = V + VG_0^+T, \quad (1)$$

where V is the sum of residual two-body interactions (potentials) for the projectile-target system, and G_0^+ is the unperturbed two-body propagator [27]. In momentum-space, the transition matrix element may be written

$$\langle \mathbf{k}' | T | \mathbf{k} \rangle = \langle \mathbf{k}' | V | \mathbf{k} \rangle + \langle \mathbf{k}' | V G_0^+ T | \mathbf{k} \rangle, \quad (2)$$

where \mathbf{k} and \mathbf{k}' are the initial and final relative momenta of the projectile-target system in the center of momentum (CM) frame, respectively. Using the notation $T(\mathbf{k}', \mathbf{k}) \equiv$

$\langle \mathbf{k}' | T | \mathbf{k} \rangle$, the momentum-space integral equation representation of the LS equation is

$$T(\mathbf{k}', \mathbf{k}) = V(\mathbf{k}', \mathbf{k}) + \int V(\mathbf{k}', \mathbf{k}'') G_0^+(k'', k) T(\mathbf{k}'', \mathbf{k}) d\mathbf{k}'', \quad (3)$$

where $k = |\mathbf{k}|$ and completeness over momenta has been used,

$$\hat{1} = \int d\mathbf{k}'' |\mathbf{k}''\rangle \langle \mathbf{k}''|. \quad (4)$$

For elastic scattering, the scattering amplitude, $f(\theta)$, is related to the transition matrix by [7]

$$f(\theta) = \frac{(-2\pi)^2 \rho}{k} T(k, \theta), \quad (5)$$

where $k = |\mathbf{k}|$, θ is the scattering angle, the density of states, ρ , is given by

$$\rho = k^2 dk / dE \quad (6)$$

and E is the energy. For non-relativistic (NR) kinematics, $E = k^2/2\mu$, where $\mu = (m_P m_T)/(m_P + m_T)$ is the reduced mass, m_P is the mass of the projectile, and m_T is the mass of the target. When using relativistic (REL) kinematics, $E = \sqrt{k^2 + m_P^2} + \sqrt{k^2 + m_T^2}$.

The total cross section is proportional to the imaginary part of the forward scattering amplitude, $\sigma_{\text{tot}} = (4\pi/k) \text{Im} [f(\theta = 0)]$, and the elastic differential cross section is found from taking the absolute square of the scattering amplitude $d\sigma/d\Omega = |f(\theta)|^2$. One simply integrates the differential cross section over the solid angle to obtain the elastic cross section, $\sigma_{\text{el}} = \int (d\sigma/d\Omega) d\Omega$. The reaction cross section, σ_{re} , can be found by subtracting the elastic cross section from the total cross section, $\sigma_{\text{re}} = \sigma_{\text{tot}} - \sigma_{\text{el}}$.

2.2 Multiple Scattering Theory

The fundamental theory which describes the interaction is MST, which was developed because the Born series proved to be inadequate due to the strong nature of the nuclear force. Watson showed that the unperturbed Hamiltonian can be separated from the sum of nucleon-nucleon interactions (residual interaction) between the projectile and target such that the leading term in the Born series can be expressed as the sum of pseudo two-body Watson- τ operators [28]. For AA scattering, the transition amplitude from equation (1) is written [27, 29]

$$T = \sum_{i=1}^{A_P} \sum_{j=1}^{A_T} T_{ij}, \quad (7)$$

where

$$T_{ij} = \tau_{ij} + \tau_{ij} G_0^+ \sum_{k \neq i}^{A_P} \sum_{l \neq j}^{A_T} T_{kl}. \quad (8)$$

A_P and A_T are the number of nucleons in the projectile and target, and the Watson- τ operator is

$$\tau_{ij} \equiv v_{ij} + v_{ij} G_0^+ \tau_{ij}. \quad (9)$$

The objective of the MST is to express the transition amplitude in terms of the free NN transition amplitude, $t_{ij} = v_{ij} + v_{ij} g t_{ij}$, where g is the free two body propagator. To that end, the pseudo two-body operator is written [27, 29]

$$\tau_{ij} = t_{ij} + t_{ij} (G_0^+ - g) \tau_{ij}. \quad (10)$$

The impulse approximation is often used and is based on the idea that the projectile has sufficiently high energy such that the target nucleon is treated as if it were free; that is, $\tau_{ij} \approx t_{ij}$, which leads to the following transition amplitude [27, 29]:

$$T_{\text{impulse}} = \sum_{i=1}^{A_P} \sum_{j=1}^{A_T} t_{ij} + \sum_{i=1}^{A_P} \sum_{j=1}^{A_T} t_{ij} G_0^+ \sum_{k \neq i}^{A_P} \sum_{l \neq j}^{A_T} t_{kl} + \dots. \quad (11)$$

The propagator G_0^+ includes the ground states and all intermediate excited states of the projectile and target. As a result, equation (11) is difficult to solve.

If elastic differential cross sections are sought, then it is convenient to separate the LS equation into an equivalent set of coupled equations with the ground state (P) and excited state (Q) projectors [8, 9]. The elastic scattering equation is

$$T = U + U P G_0^+ P T, \quad (12)$$

and the optical potential is given by

$$U = V + V Q G_0^+ Q U. \quad (13)$$

All of the intermediate excited states have been included in the optical potential. With that in mind, the Watson series for the optical potential may be written in a form similar to equations (7) and (8) [29],

$$U = \sum_{i=1}^{A_P} \sum_{j=1}^{A_T} U_{ij}, \quad (14)$$

and

$$U_{ij} = \tilde{\tau}_{ij} + \tilde{\tau}_{ij} Q G_0^+ Q \sum_{k \neq i}^{A_P} \sum_{l \neq j}^{A_T} U_{kl}, \quad (15)$$

with

$$\tilde{\tau}_{ij} \equiv v_{ij} + QG_0^+ Q \tilde{\tau}_{ij}. \quad (16)$$

Again, $\tilde{\tau}$ may be expressed in terms of the free two-body amplitude [27, 29]

$$\tilde{\tau}_{ij} = t_{ij} + t_{ij}(QG_0^+ Q - g)\tilde{\tau}_{ij}, \quad (17)$$

where the tilde notation, $\tilde{\tau}$, indicates that the pseudo two-body operators have been modified by the excited state projector, Q . If the impulse approximation is used ($\tilde{\tau}_{ij} \approx t_{ij}$), the Watson series for the optical potential becomes [29]

$$U_{\text{impulse}} = \sum_{i=1}^{A_P} \sum_{j=1}^{A_T} t_{ij} + \sum_{i=1}^{A_P} \sum_{j=1}^{A_T} t_{ij} QG_0^+ Q \sum_{k \neq i}^{A_P} \sum_{l \neq j}^{A_T} t_{kl} + \dots \quad (18)$$

Finally, if the higher order terms are neglected, and only single scattering is considered [27, 29]:

$$U_{\text{impulse}}^{\text{1st}} \approx \sum_{i=1}^{A_P} \sum_{j=1}^{A_T} t_{ij}. \quad (19)$$

At higher energies, it is assumed that higher order terms do not contribute significantly more than the single scattering term.

In all of the results that follow, $U \equiv U_{\text{impulse}}^{\text{1st}}$, and the elastic scattering equation becomes

$$T(\mathbf{k}', \mathbf{k}) = U(\mathbf{k}', \mathbf{k}) + \int \frac{U(\mathbf{k}', \mathbf{k}'')T(\mathbf{k}'', \mathbf{k})}{E(k) - E(k'') + i\epsilon} d\mathbf{k}'', \quad (20)$$

where E is the energy and $i\epsilon$ ensures outward scattering boundary conditions.

2.3 Matrix Element of Optical Potential

The explicit form of the optical potential must be defined before the solution of the LS equation can be found. The matrix element for the optical potential is written [10]

$$U(\mathbf{k}', \mathbf{k}) = \langle \mathbf{k}'; \phi_0^{A_P} \phi_0^{A_T} | U | \phi_0^{A_P} \phi_0^{A_T}; \mathbf{k} \rangle = \sum_{i=1}^{A_P} \sum_{j=1}^{A_T} \langle \mathbf{k}'; \phi_0^{A_P} \phi_0^{A_T} | t_{ij} | \phi_0^{A_P} \phi_0^{A_T}; \mathbf{k} \rangle, \quad (21)$$

where $|\phi_0^{A_P}\rangle$ and $|\phi_0^{A_T}\rangle$ are the ground states of the projectile and target, respectively. Summing over individual NN interactions, the matrix element becomes

$$U(\mathbf{k}', \mathbf{k}) = A_P A_T \langle \mathbf{k}'; \phi_0^{A_P} \phi_0^{A_T} | t | \phi_0^{A_P} \phi_0^{A_T}; \mathbf{k} \rangle. \quad (22)$$

Single scattering between a projectile and target nucleus is shown in Fig. 1. \mathbf{k} and \mathbf{k}'

are, respectively, the initial and final momenta of the projectile nucleus in the AA CM frame. Likewise, $-\mathbf{k}$ and $-\mathbf{k}'$ are the initial and final momenta of the target nucleus in the AA CM frame. The internal virtual nucleon momenta over which the integration is performed are denoted \mathbf{p}_1 and \mathbf{p}_2 . \mathbf{P}_P and \mathbf{P}_T are the momenta of the core of the $A_P - 1$ virtual projectile and $A_T - 1$ virtual target nuclei, respectively. Inserting completeness over the initial and final internal nucleon momenta and using conservation of momenta in equation (22) gives

$$U(\mathbf{k}', \mathbf{k}) = A_P A_T \int \langle \mathbf{k}'; \phi_0^{A_T} \phi_0^{A_P} | \mathbf{p}_2' \mathbf{p}_1' \rangle \langle \mathbf{p}_2' \mathbf{p}_1' | t | \mathbf{p}_2 \mathbf{p}_1 \rangle \langle \mathbf{p}_2 \mathbf{p}_1 | \mathbf{k}; \phi_0^{A_T} \phi_0^{A_P} \rangle \quad (23) \\ \times d\mathbf{p}_1' d\mathbf{p}_2' d\mathbf{p}_1 d\mathbf{p}_2 \delta(\mathbf{p}_1' - \mathbf{p}_1 - \mathbf{q}) \delta(\mathbf{p}_2' - \mathbf{p}_2 + \mathbf{q}),$$

where $\mathbf{q} = \mathbf{k}' - \mathbf{k}$ is the momentum transfer.

After evaluating the delta functions, equation (23) becomes,

$$U(\mathbf{k}', \mathbf{k}) = A_P A_T \int \langle \phi_0^{A_T} | \mathbf{p}_2 - \mathbf{q} \rangle \langle \mathbf{p}_2 | \phi_0^{A_T} \rangle \langle \phi_0^{A_P} | \mathbf{p}_1 + \mathbf{q} \rangle \langle \mathbf{p}_1 | \phi_0^{A_P} \rangle \quad (24) \\ \times \langle \mathbf{k}'; \mathbf{p}_2 - \mathbf{q}, \mathbf{p}_1 + \mathbf{q} | t | \mathbf{k}; \mathbf{p}_2, \mathbf{p}_1 \rangle d\mathbf{p}_1 d\mathbf{p}_2.$$

The notation above includes initial and final relative momenta of the projectile/target system in the CM frame, \mathbf{k} and \mathbf{k}' , and the internal nucleon momenta relative to the CM of the (projectile or target) nucleus, denoted \mathbf{p}_i , with $i = 1, 2$. These momenta (\mathbf{p}_i) are associated with the relative kinetic energy of the nucleons within the projectile (or target). The semicolon is used to show that the relative internal momenta are in a different space than the relative momenta. In the discussion that follows, \mathbf{k} and \mathbf{k}' do not change and are included for the convenience of later manipulation.

2.3.1 Optimum Factorization

Next, the optimum factorization for NA reactions in the CM frame [12, 30–32] is extended to AA reactions in the CM frame and is shown in Fig. 2, where the symmetric coordinates have been chosen for time reversal invariance [12, 30] and to allow for easier calculations. The initial momentum of the projectile nucleon is $\mathbf{p}_1 - \mathbf{q}/2$, and the final momentum is $\mathbf{p}_1 + \mathbf{q}/2$. Similarly, the initial momentum of the struck target nucleon is $\mathbf{p}_2 + \mathbf{q}/2$, and the final momentum is $\mathbf{p}_2 - \mathbf{q}/2$. It is important to note that the momenta were chosen such that $\mathbf{q} = \mathbf{k}' - \mathbf{k}$ and is the reason why the signs are reversed for the momentum transfer of the target nucleon.

The wave functions will eventually be related to the nuclear charge densities. Thus, the arguments of the wave functions will be written as arguments of the nucleon momenta relative to the cores of the $A_P - 1$ and $A_T - 1$ nuclei. Let \mathcal{P}^P be the momentum of the projectile nucleon relative to the core of the $A_P - 1$ nucleus; likewise, \mathcal{P}^T is used for the target nucleons. The initial momentum is denoted i and the final momentum is f . In

addition, if $\mathbf{K} \equiv (\mathbf{k} + \mathbf{k}')/2$ and momentum conservation from Fig. 2 are used, then the core momentum of the $A_P - 1$ virtual projectile nucleus can be expressed as $\mathbf{P}_P = \mathbf{K} - \mathbf{p}_1$. It also follows that $\mathbf{P}_T = -\mathbf{K} - \mathbf{p}_2$.

The relative momentum between particles a and b with momenta \mathbf{p}_a and \mathbf{p}_b and masses m_a and m_b is defined $\mathcal{P} \equiv (m_a \mathbf{p}_b - m_b \mathbf{p}_a)/(m_a + m_b)$. The initial relative momentum of the projectile nucleon can be found by inspection of Fig. 2. Let \mathbf{p}_a be the momentum of the core of the $A_P - 1$ nucleus ($\mathbf{p}_a = \mathbf{P}_P$), and let \mathbf{p}_b be the initial momentum of the projectile nucleon ($\mathbf{p}_b = \mathbf{p}_1 - \mathbf{q}/2$) with $m_a = A_P - 1$ and $m_b = 1$. This leads to an initial relative momentum of the projectile nucleon relative to core of the $A_P - 1$ nucleus of

$$\begin{aligned}\mathcal{P}_i^P &= \left(\frac{A_P - 1}{A_P} \right) \left[\mathbf{p}_1 - \frac{\mathbf{q}}{2} \right] - \frac{\mathbf{P}_P}{A_P} \\ &= \mathbf{p}_1 - \left(\frac{A_P - 1}{A_P} \right) \frac{\mathbf{q}}{2} - \frac{\mathbf{K}}{A_P}.\end{aligned}\tag{25}$$

Similarly, the other relative momenta may be found,

$$\begin{aligned}\mathcal{P}_f^P &= \left(\frac{A_P - 1}{A_P} \right) \left[\mathbf{p}_1 + \frac{\mathbf{q}}{2} \right] - \frac{\mathbf{P}_P}{A_P} \\ &= \mathbf{p}_1 + \left(\frac{A_P - 1}{A_P} \right) \frac{\mathbf{q}}{2} - \frac{\mathbf{K}}{A_P},\end{aligned}\tag{26}$$

$$\begin{aligned}\mathcal{P}_i^T &= \left(\frac{A_T - 1}{A_T} \right) \left[\mathbf{p}_2 + \frac{\mathbf{q}}{2} \right] - \frac{\mathbf{P}_T}{A_T} \\ &= \mathbf{p}_2 + \left(\frac{A_T - 1}{A_T} \right) \frac{\mathbf{q}}{2} + \frac{\mathbf{K}}{A_T},\end{aligned}\tag{27}$$

and

$$\begin{aligned}\mathcal{P}_f^T &= \left(\frac{A_T - 1}{A_T} \right) \left[\mathbf{p}_2 - \frac{\mathbf{q}}{2} \right] - \frac{\mathbf{P}_T}{A_T} \\ &= \mathbf{p}_2 - \left(\frac{A_T - 1}{A_T} \right) \frac{\mathbf{q}}{2} + \frac{\mathbf{K}}{A_T}.\end{aligned}\tag{28}$$

The optical potential becomes

$$U(\mathbf{k}', \mathbf{k}) = A_P A_T \int \tilde{\rho}_T(\mathcal{P}_f^T, \mathcal{P}_i^T) \tilde{\rho}_P(\mathcal{P}_f^P; \mathcal{P}_i^P) \times \langle \mathbf{k}'; \mathbf{p}_2 - \frac{\mathbf{q}}{2}, \mathbf{p}_1 + \frac{\mathbf{q}}{2} | t | \mathbf{k}; \mathbf{p}_2 + \frac{\mathbf{q}}{2}, \mathbf{p}_1 - \frac{\mathbf{q}}{2} \rangle d\mathbf{p}_1 d\mathbf{p}_2, \quad (29)$$

where $\tilde{\rho}$ is the one-nucleon (proton or neutron) density matrix of the nucleus and is related to the nuclear charge density, ρ , by [12, 30]

$$\rho(q) \equiv \tilde{\rho}\left(\frac{A-1}{A}q\right) = \int \tilde{\rho}\left(\mathbf{y} - \left[\frac{A-1}{A}\right]\frac{\mathbf{q}}{2}, \mathbf{y} + \left[\frac{A-1}{A}\right]\frac{\mathbf{q}}{2}\right) d\mathbf{y}, \quad (30)$$

where \mathbf{y} is a dummy integration variable.

It is convenient to make a change of variables by defining the following: $\mathbf{P}_1 \equiv \mathbf{p}_1 - \mathbf{K}/A_P$ and $\mathbf{P}_2 \equiv \mathbf{p}_2 + \mathbf{K}/A_T$. Then the matrix element of the optical potential becomes

$$U(\mathbf{k}', \mathbf{k}) = A_P A_T \int \tilde{\rho}_T\left(\mathbf{P}_2 - \left[\frac{A_T-1}{A_T}\right]\frac{\mathbf{q}}{2}, \mathbf{P}_2 + \left[\frac{A_T-1}{A_T}\right]\frac{\mathbf{q}}{2}\right) d\mathbf{P}_1 d\mathbf{P}_2 \times \tilde{\rho}_P\left(\mathbf{P}_1 + \left[\frac{A_P-1}{A_P}\right]\frac{\mathbf{q}}{2}, \mathbf{P}_1 - \left[\frac{A_P-1}{A_P}\right]\frac{\mathbf{q}}{2}\right) \times \langle \mathbf{k}'; \mathbf{P}_2 - \frac{\mathbf{q}}{2} - \frac{\mathbf{K}}{A_T}, \mathbf{P}_1 + \frac{\mathbf{q}}{2} + \frac{\mathbf{K}}{A_P} | t | \mathbf{k}; \mathbf{P}_2 + \frac{\mathbf{q}}{2} - \frac{\mathbf{K}}{A_T}, \mathbf{P}_1 - \frac{\mathbf{q}}{2} + \frac{\mathbf{K}}{A_P} \rangle, \quad (31)$$

where the transition amplitude is evaluated in the AA CM frame. The transition amplitude in equation (31) can be written

$$\langle \mathbf{k}'; \mathbf{P}_2 - \frac{\mathbf{q}}{2} - \frac{\mathbf{K}}{A_T}, \mathbf{P}_1 + \frac{\mathbf{q}}{2} + \frac{\mathbf{K}}{A_P} | t | \mathbf{k}; \mathbf{P}_2 + \frac{\mathbf{q}}{2} - \frac{\mathbf{K}}{A_T}, \mathbf{P}_1 - \frac{\mathbf{q}}{2} + \frac{\mathbf{K}}{A_P} \rangle = \langle \mathbf{k}'; \mathbf{k}'_2, \mathbf{k}'_1 | t | \mathbf{k}, \mathbf{k}_2; \mathbf{k}_1 \rangle, \quad (32)$$

where the initial of final projectile and target nucleon momenta in the AA CM frame are

$$\mathbf{k}_1 = \mathbf{P}_1 - \frac{\mathbf{q}}{2} + \frac{\mathbf{K}}{A_P} \quad (33)$$

$$\mathbf{k}_2 = \mathbf{P}_2 + \frac{\mathbf{q}}{2} - \frac{\mathbf{K}}{A_T} \quad (34)$$

$$\mathbf{k}'_1 = \mathbf{P}_1 + \frac{\mathbf{q}}{2} + \frac{\mathbf{K}}{A_P} \quad (35)$$

$$\mathbf{k}'_2 = \mathbf{P}_2 - \frac{\mathbf{q}}{2} - \frac{\mathbf{K}}{A_T} \quad (36)$$

The current work uses parameterizations of NN amplitudes to predict NA and AA differential cross sections. Consequently, the quantity that allows for the transformation of the transition amplitude from the AA CM frame the NN CM frame, known as the Möller factor (η) [7, 33], must be found.

The Moller transformation factor can be found by examining the Lorentz invariant (LI) cross section, which is written [7, 12]

$$d\sigma = \int \frac{d\mathbf{k}'_1}{E'_1} \frac{d\mathbf{k}'_2}{E'_2} \delta(E - E') \delta(\mathbf{P} - \mathbf{P}') \frac{(2\pi)^4}{B} |M_{12}|^2, \quad (37)$$

with

$$M_{12} = \sqrt{E'_1 E'_2} T_{12} \sqrt{E_1 E_2}, \quad (38)$$

where E and \mathbf{P} are the initial total energy and momentum of the system, E' and \mathbf{P}' are the final total energy and momentum of the system, E_1 and E_2 are the total energies of the two particles before the collision, E'_1 and E'_2 are the total energies of the two particles after the collision, \mathbf{k}_1 and \mathbf{k}_2 are the initial momenta of the two particles, \mathbf{k}'_1 and \mathbf{k}'_2 are the final momenta of the two particles, and $B = \frac{1}{2} \sqrt{\lambda(s, m_1^2, m_2^2)}$, where

$$\lambda(s, m_1^2, m_2^2) = (s - m_1^2 - m_2^2)^2 - 4m_1^2 m_2^2. \quad (39)$$

Since, $d\mathbf{k}_i/E_i$, $\delta(E - E')\delta(\mathbf{P} - \mathbf{P}')$, B , and $d\sigma$ are LI, then M_{12} is LI. Thus,

$$[M_{12}]_{AA} = [M_{12}]_{NN}. \quad (40)$$

The initial and final relative momenta of projectile and target nucleons in the NN CM frame can be expressed as

$$\tilde{\mathbf{k}} \equiv -\frac{1}{2} \left[\left(\mathbf{P}_2 + \frac{\mathbf{q}}{2} - \frac{\mathbf{K}}{A_T} \right) - \left(\mathbf{P}_1 - \frac{\mathbf{q}}{2} + \frac{\mathbf{K}}{A_P} \right) \right] \quad (41)$$

and

$$\tilde{\mathbf{k}}' \equiv -\frac{1}{2} \left[\left(\mathbf{P}_2 - \frac{\mathbf{q}}{2} - \frac{\mathbf{K}}{A_T} \right) - \left(\mathbf{P}_1 + \frac{\mathbf{q}}{2} + \frac{\mathbf{K}}{A_P} \right) \right]. \quad (42)$$

Using equation (38), the AA CM frame is related to the NN CM frame by

$$\begin{aligned} & \sqrt{E_N(\mathbf{k}'_2) E_N(\mathbf{k}'_1)} \langle \mathbf{k}'_2, \mathbf{k}'_1 | t | \mathbf{k}_2, \mathbf{k}_1 \rangle_{AA} \sqrt{E_N(\mathbf{k}_2) E_N(\mathbf{k}_1)} \\ &= \sqrt{E_N(\tilde{\mathbf{k}}') E_N(-\tilde{\mathbf{k}}')} \langle \mathbf{k}'_2, \tilde{\mathbf{k}}', -\tilde{\mathbf{k}}' | t | \mathbf{k}_2, \tilde{\mathbf{k}}, -\tilde{\mathbf{k}} \rangle_{NN} \sqrt{E_N(\tilde{\mathbf{k}}) E_N(-\tilde{\mathbf{k}})}. \end{aligned} \quad (43)$$

Therefore, $\langle t \rangle_{AA} = \eta \langle t \rangle_{NN}$, where

$$\eta = \sqrt{\frac{E_N(\tilde{\mathbf{k}}') E_N(-\tilde{\mathbf{k}}') E_N(\tilde{\mathbf{k}}) E_N(-\tilde{\mathbf{k}})}{E_N(\mathbf{k}'_2) E_N(\mathbf{k}'_1) E_N(\mathbf{k}_2) E_N(\mathbf{k}_1)}}, \quad (44)$$

The notation can be simplified by defining

$$\mathbf{Y} \equiv \frac{1}{2}(\tilde{\mathbf{k}} + \tilde{\mathbf{k}}') = \frac{1}{2} \left[\frac{\mathbf{K}}{A_T} - \mathbf{P}_2 + \frac{\mathbf{K}}{A_P} + \mathbf{P}_1 \right] \quad (45)$$

such that

$$\langle \mathbf{k}'_2, \mathbf{k}'_1 | t | \mathbf{k}_2, \mathbf{k}_1 \rangle_{AA} = \eta t_{NN}(\mathbf{q}; -2\mathbf{Y}, 2\mathbf{Y}). \quad (46)$$

and

$$\begin{aligned} U(\mathbf{k}', \mathbf{k}) &= A_P A_T \int \tilde{\rho}_T \left(\mathbf{P}_2 - \left[\frac{A_T - 1}{A_T} \right] \frac{\mathbf{q}}{2}, \mathbf{P}_2 + \left[\frac{A_T - 1}{A_T} \right] \frac{\mathbf{q}}{2} \right) \\ &\quad \times \tilde{\rho}_P \left(\mathbf{P}_1 + \left[\frac{A_P - 1}{A_P} \right] \frac{\mathbf{q}}{2}, \mathbf{P}_1 - \left[\frac{A_P - 1}{A_P} \right] \frac{\mathbf{q}}{2} \right) \eta t_{NN}(\mathbf{q}; -2\mathbf{Y}, 2\mathbf{Y}) d\mathbf{P}_1 d\mathbf{P}_2. \end{aligned} \quad (47)$$

The NN transition amplitude may be written as a function of \mathbf{q} and $\mathbf{Y}(\mathbf{P}_1, \mathbf{P}_2)$ without loss of generality.

Since the size of the nucleus is much larger than the range of the NN interaction, the transition amplitude varies more slowly with \mathbf{P}_1 and \mathbf{P}_2 when compared to the one nucleon density matrix for the nucleus [12, 30]. For this reason, the NN transition amplitude is evaluated at fixed values of \mathbf{P}_1 and \mathbf{P}_2 , namely $\mathbf{P}_1 = \mathbf{P}_{10}$ and $\mathbf{P}_2 = \mathbf{P}_{20}$. The optimum values of \mathbf{P}_{10} and \mathbf{P}_{20} are estimated by expanding the transition amplitude in a Taylor series and requiring second-order terms (and higher) to be zero. After the optimum values are found, the optical potential for elastic scattering is stated for central potentials.

The transition amplitude may be expanded as

$$\begin{aligned}
t_{\text{NN}}(\mathbf{q}; 2\mathbf{Y}) &\approx t_{\text{NN}}(\mathbf{q}; \frac{\mathbf{K}}{A_T} - \mathbf{P}_{20} + \frac{\mathbf{K}}{A_P} + \mathbf{P}_{10}) \\
&+ \frac{\partial}{\partial \mathbf{P}_{20}} t_{\text{NN}}(\mathbf{q}; \frac{\mathbf{K}}{A_T} - \mathbf{P}_{20} + \frac{\mathbf{K}}{A_P} + \mathbf{P}_{10})(\mathbf{P}_2 - \mathbf{P}_{20}) \\
&+ \frac{\partial}{\partial \mathbf{P}_{10}} t_{\text{NN}}(\mathbf{q}; \frac{\mathbf{K}}{A_T} - \mathbf{P}_{20} + \frac{\mathbf{K}}{A_P} + \mathbf{P}_{10})(\mathbf{P}_1 - \mathbf{P}_{10}) + \theta(\mathbf{P}_1, \mathbf{P}_2),
\end{aligned} \tag{48}$$

where θ represents higher order terms. Using equation (30) and the Taylor series expansion leads to the following matrix element of the optical potential:

$$\begin{aligned}
U(\mathbf{k}', \mathbf{k}) &= A_P A_T \eta t_{\text{NN}}(\mathbf{q}; \frac{\mathbf{K}}{A_T} - \mathbf{P}_{20} + \frac{\mathbf{K}}{A_P} + \mathbf{P}_{10}) \rho_T(q) \rho_P(q) \\
&+ \left[A_P A_T \frac{\partial}{\partial \mathbf{P}_{20}} t_{\text{NN}}(\mathbf{q}; \frac{\mathbf{K}}{A_T} - \mathbf{P}_{20} + \frac{\mathbf{K}}{A_P} + \mathbf{P}_{10}) \right] \\
&\quad \times \left[\int (\mathbf{P}_2 - \mathbf{P}_{20}) \tilde{\rho}_T(\mathbf{P}_2, \mathbf{q}) \tilde{\rho}_P(\mathbf{P}_1, \mathbf{q}) d\mathbf{P}_1 d\mathbf{P}_2 \right] \\
&+ \left[A_P A_T \frac{\partial}{\partial \mathbf{P}_{10}} t_{\text{NN}}(\mathbf{q}; \frac{\mathbf{K}}{A_T} - \mathbf{P}_{20} + \frac{\mathbf{K}}{A_P} + \mathbf{P}_{10}) \right] \\
&\quad \times \left[\int (\mathbf{P}_1 - \mathbf{P}_{10}) \tilde{\rho}_T(\mathbf{P}_2, \mathbf{q}) \tilde{\rho}_P(\mathbf{P}_1, \mathbf{q}) d\mathbf{P}_1 d\mathbf{P}_2 \right] + \dots
\end{aligned} \tag{49}$$

The optimum values for \mathbf{P}_{20} and \mathbf{P}_{10} can be estimated by requiring the second order terms in the Taylor series expansion to be zero [12]; that is,

$$\int (\mathbf{P}_2 - \mathbf{P}_{20}) \tilde{\rho}_T(\mathbf{P}_2, \mathbf{q}) \tilde{\rho}_P(\mathbf{P}_1, \mathbf{q}) d\mathbf{P}_1 d\mathbf{P}_2 = 0 \tag{50}$$

and

$$\int (\mathbf{P}_1 - \mathbf{P}_{10}) \tilde{\rho}_T(\mathbf{P}_2, \mathbf{q}) \tilde{\rho}_P(\mathbf{P}_1, \mathbf{q}) d\mathbf{P}_1 d\mathbf{P}_2 = 0. \tag{51}$$

Equation (50) can be written as

$$\mathbf{P}_{20} \rho_T(q) \rho_P(q) = \int \rho_P(q) \tilde{\rho}_T(\mathbf{P}_2, \mathbf{q}) \mathbf{P}_2 d\mathbf{P}_2. \tag{52}$$

The single particle density matrix for the nucleus is derived from the ground state wave function, which is a symmetric function of its coordinates and invariant under the parity transformation ($\mathbf{P}_2 \rightarrow -\mathbf{P}_2$) [12], since the strong interaction preserves parity. Likewise, the entire integral is invariant under a parity transformation and evaluates to zero; thus, $\mathbf{P}_{20} = \mathbf{0}$. The same argument follows for the second term of the matrix element of the

optical potential and $\mathbf{P}_{10} = \mathbf{0}$. Using these values for \mathbf{P}_{10} and \mathbf{P}_{20} leads to

$$U(\mathbf{k}', \mathbf{k}) = A_P A_T \eta t_{\text{NN}} \left[\mathbf{q}; \left(\frac{A_P + A_T}{A_P A_T} \right) \mathbf{K} \right] \rho_T(q) \rho_P(q). \quad (53)$$

Only central potentials have been considered; that is, the effects of spin are ignored. As a result, the interaction must be a function of the possible scalar products in equation (53): $\mathbf{q} \cdot \mathbf{q}$, $\mathbf{q} \cdot \mathbf{K}$, and $\mathbf{K} \cdot \mathbf{K}$. Using $|\mathbf{k}| = |\mathbf{k}'|$ for elastic scattering, one can show that

$$U(\mathbf{k}', \mathbf{k}) = A_P A_T \eta t_{\text{NN}}(e_{\text{NN}}, q) \rho_T(q) \rho_P(q), \quad (54)$$

where e_{NN} is the NN CM kinetic energy. The current work uses an NN transition amplitude that is evaluated at the energy available per nucleon that is related to the fixed beam energy [11].

In the next section, the eikonal approximation is discussed, and exact formulas for the optical potential are given in position-space with the transition amplitude and harmonic well densities described in Appendices A and B.

2.4 Eikonal Solution Method

The eikonal approximation is used for high energy, small angle scattering to calculate elastic, reaction, total, and elastic differential cross sections [7, 34]. To compute cross sections with the eikonal method, one solves for the eikonal scattering amplitude, $f(\theta)$, which is given as [7]

$$f(\theta) = \frac{k}{i} \int_0^\infty J_0(2k \sin(\theta/2)) [e^{i\chi(k,b)} - 1] b \, db, \quad (55)$$

where k is the relative momentum of the projectile-target system in the CM frame, J_0 is the ordinary cylindrical Bessel function, θ is the scattering angle in the CM frame, b is the impact parameter, and $\chi(k, b)$ is the eikonal phase shift function, which is obtained by integrating over the optical potential, $U(b, z)$ [7]:

$$\chi(k, b) = -\frac{1}{2k} \int_{-\infty}^\infty U(b, z) dz. \quad (56)$$

The z -integration is taken to be in the same direction as the initial wave vector of the incident projectile. The elastic differential cross section is found by taking the absolute square of the scattering amplitude, $d\sigma/d\Omega = |f(\theta)|^2$.

Since the eikonal approximation satisfies the optical theorem, the total cross section

is proportional to the imaginary part of the forward scattering amplitude,

$$\sigma_{\text{tot}} = \frac{4\pi}{k} \text{Im} f(\theta = 0) = 4\pi \int_0^\infty [1 - e^{-\text{Im}\chi} \cos(\text{Re}\chi)] b \, db. \quad (57)$$

The total elastic cross section, σ_{el} , is obtained by integrating the elastic differential cross section [7],

$$\begin{aligned} \sigma_{\text{el}} = \int \frac{d\sigma}{d\Omega} d\Omega &= 4\pi \int_0^\infty [1 - e^{-\text{Im}\chi} \cos(\text{Re}\chi)] b \, db \\ &\quad - 2\pi \int_0^\infty [1 - e^{-2\text{Im}\chi}] b \, db, \end{aligned}$$

and the reaction cross section, σ_{re} , is found by using $\sigma_{\text{re}} = \sigma_{\text{tot}} - \sigma_{\text{el}}$; thus,

$$\sigma_{\text{re}} = 2\pi \int_0^\infty [1 - e^{-2\text{Im}\chi}] b \, db. \quad (58)$$

All of the cross sections described above are functions of the eikonal phase function and depend on the optical potential, as shown in equation (56). For AA scattering, the optical potential may be expressed as [5, 16]

$$U(\mathbf{r}) = A_P A_T \int t_{\text{NN}}(|\mathbf{r}_{\text{NN}}|) \rho_P(|\mathbf{r}_P|) \rho_T(|\mathbf{r}_T|) \, d\mathbf{r}_T d\mathbf{r}_{\text{NN}}, \quad (59)$$

where A is the number of nucleons, P represents the projectile, T represents the target, t_{NN} is the NN transition amplitude, and ρ is the nuclear matter density. \mathbf{r}_{NN} is the vector between a nucleon in the projectile and a nucleon in the target, \mathbf{r}_P is the vector that extends from the center of the projectile nucleus to a nucleon in the projectile, \mathbf{r}_T is the vector between the center of the target nucleus to a nucleon in the target, \mathbf{r} is the relative distance between the centers of the projectile and target nuclei, $\mathbf{R} = \mathbf{r} + \mathbf{r}_T$ is the distance from the center of the projectile to a nucleon in the target. The distance from the center of the projectile nucleus to a nucleon in the projectile may be expressed as $\mathbf{r}_P = \mathbf{r} + \mathbf{R} = \mathbf{r} + \mathbf{r}_T + \mathbf{r}_{\text{NN}}$, which, when substituted into equation (59), leads to

$$U(\mathbf{r}) = A_P A_T \int t_{\text{NN}}(|\mathbf{r}_{\text{NN}}|) \rho_P(|\mathbf{r} + \mathbf{r}_T + \mathbf{r}_{\text{NN}}|) \rho_T(|\mathbf{r}_T|) d\mathbf{r}_T d\mathbf{r}_{\text{NN}}. \quad (60)$$

(Note that $|\mathbf{r}| = \sqrt{b^2 + z^2}$ in the cylindrical coordinate system.) The vectors used in this

discussion of the AA optical potential are illustrated in Fig. 3.

In the next two sections, analytic expressions for the optical potential are presented for nuclei with $A \leq 16$, where harmonic-well nuclear matter densities have been used. Harmonic well densities [5] are given by

$$\rho^{\text{HW}}(r) = (\alpha + \beta r^2) \exp\left[\frac{-r^2}{4s^2}\right], \quad (61)$$

and the NN transition amplitude is [5]

$$t_{\text{NN}}(r) = \tau \exp\left[\frac{-r^2}{2B(e)}\right]. \quad (62)$$

(See Appendices A and B for a full description of the densities and transition amplitudes used in the current work.)

2.4.1 Nucleon-Nucleus Optical Potential

For NA collisions, the single projectile nucleon charge density is taken as a Dirac delta function, and the harmonic-well nuclear matter density is used for the target. Thus, the exact optical potential from equation (60) may be expressed in the following form with $A_P = 1$:

$$U(r) = (C_0 + C_1 r^2) \exp[-C_2 r^2] \quad (63)$$

with

$$C_0 = \tau A_T \left(\frac{\pi}{\mu_1 + \mu_2} \right)^{3/2} \left[\alpha_T + \frac{3\beta_T}{2(\mu_1 + \mu_2)} \right], \quad (64)$$

$$C_1 = \frac{\tau \beta_T A_T \mu_1^2 \pi^{3/2}}{(\mu_1 + \mu_2)^{7/2}}, \quad (65)$$

and

$$C_2 = \mu_1 - \frac{\mu_1^2}{(\mu_1 + \mu_2)}, \quad (66)$$

where

$$\mu_1 = \frac{1}{2B} \quad \text{and} \quad \mu_2 = \frac{1}{4s_T^2}. \quad (67)$$

2.4.2 Nucleus-Nucleus Optical Potential

The calculation of the optical potential is repeated for AA collisions with harmonic-well nuclear charge densities for both the projectile and the target, which results in the following formula for the optical potential:

$$U(r) = (A_0 + A_1 r^2 + A_2 r^4) \exp[-A_3 r^2], \quad (68)$$

where

$$\begin{aligned} A_0 = & \frac{2\pi N A_P A_T}{\theta} \sqrt{\frac{\pi}{\theta}} \\ & \times \left[\frac{\alpha_T \Lambda_1}{2} + \frac{3}{4\theta} (\beta_T \Lambda_1 + \Lambda_2 \alpha_T) \right. \\ & \left. + \frac{15\Lambda_2 \beta_T}{8\theta^2} \right], \end{aligned} \quad (69)$$

$$\begin{aligned} A_1 = & \frac{2\pi N A_P A_T}{\theta} \sqrt{\frac{\pi}{\theta}} \\ & \times \left[\frac{\alpha_T \Lambda_2}{2} + \frac{1}{4\theta} (3\Lambda_2 \beta_T - 4\alpha_T \Lambda_2 \delta) \right. \\ & + \frac{\delta}{2\theta^2} (\beta_T \Lambda_1 \delta + \Lambda_2 \alpha_T \delta - 5\beta_T \Lambda_2) \\ & \left. + \frac{5\delta^2 \Lambda_2 \beta_T}{2\theta^3} \right], \end{aligned} \quad (70)$$

$$\begin{aligned} A_2 = & \frac{2\pi N A_P A_T}{\theta} \sqrt{\frac{\pi}{\theta}} \\ & \times \left[\frac{\Lambda_2 \beta_T \delta^2}{2\theta^2} - \frac{\beta_T \Lambda_2 \delta^3}{\theta^3} + \frac{\Lambda_2 \beta_T \delta^4}{2\theta^4} \right], \end{aligned} \quad (71)$$

and

$$A_3 = \delta - \frac{\delta^2}{\theta}, \quad (72)$$

where

$$N = \frac{2\pi\tau}{\kappa} \sqrt{\frac{\pi}{\kappa}}, \quad (73)$$

$$\kappa = \frac{1}{4s_P^2} + \frac{1}{2B}, \quad (74)$$

$$\theta = \frac{1}{4s_T^2} + \delta, \quad (75)$$

$$\delta = \frac{1}{4s_P^2} - \frac{1}{16s_P^4\kappa}, \quad (76)$$

$$\Lambda_1 = \frac{\alpha_P}{2} + \frac{3\beta_P}{4\kappa}, \quad (77)$$

and

$$\Lambda_2 = \frac{\beta_P}{2} + \frac{\beta_P}{32\kappa^2 s_P^4} - \frac{\beta_P}{4\kappa s_P^2}. \quad (78)$$

These results have been derived independently by Townsend and Bidasaria [35, 36]. In the next section, the optical potential is written as a function of momentum transfer, which leads to more efficient evaluation of cross sections when exact expressions for the optical potential are not known.

2.4.3 Optical Potential in Momentum-Space

In section 2.2, it was shown that the phase function is obtained by integrating the optical potential in the position-space representation. In this section, the phase shift function is written such that the optical potential is expressed as a function of momentum transfer \mathbf{q} . By doing so, the number of integration dimensions will be significantly reduced.

To begin, the NN transition amplitude and nuclear charge densities in equation (60) are replaced with their Fourier transforms

$$U(\mathbf{r}) = \frac{A_P A_T}{(2\pi)^6} \int d\mathbf{r}_T d\mathbf{r}_{\text{NN}} d\mathbf{q}_1 d\mathbf{q}_2 d\mathbf{q}_3 [t_{\text{NN}}(|\mathbf{q}_1|) \rho_T(|\mathbf{q}_2|) \rho_P(|\mathbf{q}_3|) \times e^{-i\mathbf{q}_1 \cdot \mathbf{r}_{\text{NN}}} e^{-i\mathbf{q}_2 \cdot \mathbf{r}_T} e^{-i\mathbf{q}_3 \cdot (\mathbf{r} + \mathbf{r}_T + \mathbf{r}_{\text{NN}})}], \quad (79)$$

where the Fourier transforms are given by

$$t_{\text{NN}}(\mathbf{r}) = \frac{1}{(2\pi)^3} \int t_{\text{NN}}(\mathbf{q}) e^{-i\mathbf{q} \cdot \mathbf{r}} d\mathbf{q}, \quad (80)$$

and

$$\rho(\mathbf{r}) = \int \rho(\mathbf{q}) e^{-i\mathbf{q} \cdot \mathbf{r}} d\mathbf{q}. \quad (81)$$

The normalizations for the Fourier transforms of $\rho(\mathbf{r})$ and $t_{\text{NN}}(\mathbf{r})$ differ because of the traditional normalization of nuclear charge densities. Next, integration over \mathbf{r}_T and \mathbf{r}_{NN} is performed with the Dirac delta function,

$$\delta(\mathbf{A}) = \frac{1}{(2\pi)^3} \int e^{-i\mathbf{A} \cdot \mathbf{B}} d\mathbf{B}, \quad (82)$$

which results in

$$U(\mathbf{r}) = A_P A_T \int t_{\text{NN}}(|\mathbf{q}_1|) \rho_T(|\mathbf{q}_2|) \rho_P(|\mathbf{q}_3|) \delta(\mathbf{q}_1 - \mathbf{q}_3) \delta(\mathbf{q}_1 + \mathbf{q}_2) e^{-i\mathbf{q}_3 \cdot \mathbf{r}} d\mathbf{q}_1 d\mathbf{q}_2 d\mathbf{q}_3. \quad (83)$$

After evaluating the delta functions, the optical potential is reduced to integration over the momentum transfer,

$$U(\mathbf{r}) = \int U(\mathbf{q}) e^{-i\mathbf{q} \cdot \mathbf{r}} d\mathbf{q}, \quad (84)$$

where $U(\mathbf{q}) = A_P A_T t_{\text{NN}}(|\mathbf{q}|) \rho_P(|\mathbf{q}|) \rho_T(|\mathbf{q}|)$.

Next, the Fourier transform of the optical potential (84) is substituted into the expression for the eikonal phase shift function from equation (56),

$$\begin{aligned} \chi(k, b) &= -\frac{1}{2k} \int_{-\infty}^{\infty} dz \int U(\mathbf{q}) e^{-i\mathbf{q} \cdot (\mathbf{z} + \mathbf{b})} d\mathbf{q} \\ &= -\frac{1}{2k} \int_{-\infty}^{\infty} dz \int d\mathbf{q} U(\mathbf{q}) e^{-i\mathbf{q} \cdot \mathbf{b}} e^{-iqz \cos \theta}, \end{aligned} \quad (85)$$

where $\mathbf{r} = \mathbf{b} + \mathbf{z}$ in cylindrical coordinates has been used. The integration of z is performed, which results in

$$\chi(k, b) = -\frac{\pi}{k} \int \frac{1}{q} \delta(\cos \theta) U(\mathbf{q}) e^{-i\mathbf{q} \cdot \mathbf{b}} d\mathbf{q}, \quad (86)$$

where the following delta function has been used,

$$\frac{2\pi}{q} \delta(\cos \theta) = \int_{-\infty}^{\infty} e^{-iqz \cos \theta} dz. \quad (87)$$

Using $d\mathbf{q} = q^2 dq \sin \theta d\theta d\phi$ and evaluating the delta functions leads to the final form for the eikonal phase function,

$$\chi(k, b) = -\frac{\pi}{k} \int_0^{\infty} dq \int_0^{2\pi} q U(|\mathbf{q}|) e^{-iqb \cos \phi} d\phi. \quad (88)$$

The advantage of equation (88) is that the optical potential is in the momentum-space representation, and the z -integration need not be performed. Instead, the 7-dimensional integral for χ has been reduced to 2-dimensions over the magnitude of the momentum transfer, q , and the angle, ϕ , between the momentum transfer and the impact parameter. This result significantly increases the efficiency for the numerical evaluation of χ .

2.5 Lippmann-Schwinger Partial Wave Solution Method

The LS equation is often solved with the method of partial waves, a well-known method that is described in standard texts [7, 37]. An overview of the method is presented here.

Equation (20) is solved with the partial wave method using the optical potential from equation (54). Any function, Z , can be expanded in a complete orthonormal set of basis functions,

$$Z(\mathbf{q}) = Z(\mathbf{k}', \mathbf{k}) = \sum_{l=0}^{\infty} \sum_{m=-l}^l Z_l(k', k) Y_l^{m*}(\hat{k}') Y_l^m(\hat{k}) \quad (89)$$

$$= \sum_{l=0}^{\infty} \frac{2l+1}{4\pi} Z_l(k', k) P_l(x), \quad (90)$$

where $\mathbf{q} = \mathbf{k}' - \mathbf{k}$ is the momentum transfer, $Y_l^{m*}(\hat{k}')$ and $Y_l^m(\hat{k})$ are spherical harmonics, \hat{k} and \hat{k}' represent the polar and azimuthal angles associated with \mathbf{k} and \mathbf{k}' , respectively; $P_l(x)$ are the Legendre polynomials, and $x = \cos(\theta_{kk'})$, where $\theta_{kk'}$ is the angle between \mathbf{k} and \mathbf{k}' . After expanding T and U , one integrates out the angular dependence, which leads to the PW LS equation

$$T_l(k', k) = U_l(k', k) + \int_0^{\infty} \frac{U_l(k', k'') T_l(k'', k)}{E(k) - E(k'') + i\epsilon} k''^2 dk'', \quad (91)$$

where

$$U_l(k', k) = 2\pi \int_{-1}^1 U(q) P_l(x) dx. \quad (92)$$

A common way of solving the above equation is through the R -matrix, which consists of a principal value integral. When expanded in partial waves, R_l has a form similar to T_l above,

$$R_l(k', k) = U_l(k', k) + \mathbf{P} \int_0^{\infty} \frac{U_l(k', k'') R_l(k'', k)}{E(k) - E(k'')} k''^2 dk'', \quad (93)$$

where \mathbf{P} represents the principal value integral. The Heitler equation may be used to obtain $T_l(k', k)$,

$$T_l(k', k) = \frac{R_l(k', k)}{1 + i\pi\rho R_l(k', k)}, \quad (94)$$

where ρ is given in equation (6). The final step is to re-sum the infinite series,

$$T(\mathbf{q}) = \langle \mathbf{k}' | T | \mathbf{k} \rangle = \sum_{l=0}^{\infty} \frac{2l+1}{4\pi} T_l(k', k) P_l(x). \quad (95)$$

It was recently demonstrated that elastic scattering finite sum expressions converge more quickly than the infinite series above [21]. The derivation is based on the idea that the Born approximation becomes sufficient for some large angular momentum; that is, for $l > l_{\max}$, $T_l(k, k) \approx U_l(k, k)$. Using this idea, the finite sum expression for the scattering amplitude is [10, 12, 21, 38]

$$f(\theta) = -(2\pi)^2 \frac{\rho}{k} \sum_{l=0}^{l_{\max}} \frac{2l+1}{4\pi} [T_l(k, k) - U_l(k, k)] P_l(x) - (2\pi)^2 \frac{\rho}{k} U(q). \quad (96)$$

The total cross section is proportional to the imaginary part of the forward scattering amplitude [21],

$$\sigma_{\text{tot}} = -16\pi^3 \frac{\rho}{k^2} \sum_{l=0}^{l_{\max}} \frac{2l+1}{4\pi} \text{Im}[T_l(k, k) - U_l(k, k)] + \sigma_{\text{tot}}^{\text{Born}}, \quad (97)$$

where $\sigma_{\text{tot}}^{\text{Born}}$ is the total cross section in the Born approximation. The elastic cross section is derived from taking the absolute square of the elastic differential cross section [21],

$$\sigma_{\text{el}} = \frac{(2\pi)^4 \rho^2}{k^2} \left[\sum_{l=0}^{l_{\max}} \frac{2l+1}{4\pi} \left(|T_l|^2 - |U_l|^2 \right) \right] + \sigma_{\text{el}}^{\text{Born}}, \quad (98)$$

where

$$\sigma_{\text{el}}^{\text{Born}} = \int | - (2\pi)^2 \frac{\rho}{k} U(q) |^2 d\Omega, \quad (99)$$

and the reaction cross section is obtained by subtracting the elastic cross section from the total cross section.

2.6 Lippmann-Schwinger 3D Solution Method

The LS3D solution method avoids the numerical difficulties associated with the PW method and has been used for relatively low energy reactions [22–26]. This section reviews the LS3D method as it has been described in the work of Elster et al. [22] and Rodriguez-Gallardo et al. [24].

If one considers only central potentials in equation (3), then both T and V are scalar functions; that is, $f(\mathbf{k}', \mathbf{k}) = f(k', k, \hat{k}' \cdot \hat{k})$ for some function f , where \hat{k} (\hat{k}') represents

the angular unit vectors associated with \mathbf{k} (\mathbf{k}'). The possible scalar products of the LS equation are as follows [22, 24]:

$$\begin{aligned} x' &\equiv \hat{k}' \cdot \hat{k} \\ x'' &\equiv \hat{k}'' \cdot \hat{k} \\ y &\equiv \hat{k}'' \cdot \hat{k}'. \end{aligned} \quad (100)$$

The incoming momentum, \mathbf{k} , is taken to be in the direction of the z -axis, and the azimuthal angle between \mathbf{k} and \mathbf{k}' is set to zero: $\phi' = 0$; therefore, y may be expressed as a function of x' , x'' , and ϕ'' [22, 24],

$$y = x'x'' + \sqrt{1-x'^2}\sqrt{1-x''^2}\cos\phi''. \quad (101)$$

Note that only $U(k', k'', y)$ is dependent on ϕ'' ; therefore [22],

$$\bar{U}(k', x', k'', x'') \equiv \int_0^{2\pi} U(k', k'', y) d\phi'', \quad (102)$$

and the LS equation becomes [22]

$$\begin{aligned} T(k', k, x') &= U(k', k, x') \\ &+ \int_0^\infty k''^2 dk'' \int_{-1}^1 dx'' \frac{\bar{U}(k', x', k'', x'') T(k'', k, x'')}{E(k) - E(k'') + i\epsilon}. \end{aligned} \quad (103)$$

The propagator may be expressed as [37]

$$\lim_{\eta \rightarrow 0} \frac{1}{E(k) - E(k'') + i\epsilon} = \mathbf{P} \left(\frac{1}{E(k) - E(k'')} \right) - i\pi\delta(E(k) - E(k'')), \quad (104)$$

where \mathbf{P} is the principal value. The LS equation becomes (after suppressing the on-shell momentum in T and V)

$$\begin{aligned} T(k', x') &= U(k', x') + \mathbf{P} \int \frac{\bar{U}(k', x', k'', x'') T(k'', x'') k''^2 dk'' dx''}{E(k) - E(k'')} \\ &- i\pi \int \bar{U}(k', x', k'', x'') T(k'', x'') k''^2 dk'' dx'' \delta(E(k) - E(k'')). \end{aligned} \quad (105)$$

Next, the delta function is evaluated, and the kinematic factors are specified. The NR energy is $E = k^2/2\mu$, where μ is the reduced mass of the projectile-target system, and

k is the relative momentum of the projectile-target system in the AA CM frame. The REL energy is $E = E_P + E_T$, where $E_P = \sqrt{m_P^2 + k^2}$ and $E_T = \sqrt{m_T^2 + k^2}$. P denotes projectile, and T denotes target. The delta function may be expressed as

$$\delta(E(k) - E(k'')) = \frac{\delta(k - k'')}{\left| \frac{dE}{dk} \right|_{(k''=k)}} = \frac{\mu^{\text{kin}}}{k} \delta(k - k''), \quad (106)$$

where negative momenta have been disregarded, kin represents non-relativistic (NR) or relativistic (REL) kinematics, and

$$\mu^{\text{kin}} = \begin{cases} \frac{m_P m_T}{m_P + m_T} & \text{for non-relativistic kinematics} \\ \frac{E_P E_T}{E_P + E_T} & \text{for relativistic kinematics.} \end{cases} \quad (107)$$

After evaluating the delta function, equation (105) becomes

$$\begin{aligned} T(k', x') = U(k', x') + \mathbf{P} \int \frac{\bar{U}(k', x', k'', x'') T(k'', x'')}{E(k) - E(k'')} k''^2 dk'' dx'' \\ - i\pi \mu^{\text{kin}} \int \bar{U}(k', x', k, x'') T(k, x'') k dx''. \end{aligned} \quad (108)$$

Equation (108) is solved with the numerical methods described in the next section.

3 Numerical Methods

Thus far, three different solution methods for the LS equation have been presented, including the eikonal approximation, the PW, and LS3D solution methods. This section describes the numerical techniques used to implement the three methods.

3.1 Eikonal

Exact formulas for the optical potentials in equations (63) and (68) are used for light nuclei reactions ($A \leq 16$). For reactions with heavier nuclei ($A > 16$), the momentum-space representation of the eikonal phase function described in equation (88) is implemented. Although the momentum space method for the eikonal phase function is much more efficient than the position space calculation, additional interpolation over the impact parameter and momentum transfer was performed for additional numerical efficiency. Convergence of the total elastic cross sections was used to establish the number of Gaussian quadrature points used for integration. The number of Gaussian quadrature points for the eikonal solution method was increased to a maximum of 100 points such that the total elastic

cross sections changed less than 1% for all reactions with energies up to 100 GeV/n.

3.2 Partial Wave Lippmann-Schwinger

As discussed in the last section, one may first solve for the l th PW of the R -matrix, equation (93), and then find T_l from the Heitler equation. The transition matrix is found by performing the sum in equation (95). To solve for R_l , an even number of Gaussian quadrature points, N , is used to perform the integration of the momentum; thus, equation (93) becomes

$$R_l(k', k) = U_l(k', k) + \sum_{k''=1}^N \frac{U_l(k', k'') R_l(k'', k) k''^2 w_{k''}}{E(k) - E(k'')}, \quad (109)$$

where k'' now represents a discrete Gaussian quadrature transformed index, and $w_{k''}$ is the corresponding weight for the integrated variable. Note that a principal value singularity will occur in the propagator when $k'' = k$ and may be removed by implementing a subtraction scheme [37] or the method of Sloan [39]. Sloan's method requires that the pole be placed at the center of an even number of Gaussian quadrature points when integrated. Since the pole occurs at $k'' = k$, the limits of integration are divided into two parts: $[0, \infty) \rightarrow [0, 2k]$ and $[2k, \infty)$. By placing the pole in the center of the interval $[0, 2k]$, and by using an even number of Gaussian quadrature points, the principal value singularity is removed.

To isolate R_l , the above equation is written

$$\sum_{k''=1}^N \Lambda(k', k'') R_l(k'', k) = U_l(k', k), \quad (110)$$

where

$$\Lambda(k', k'') = \delta_{k', k''} - \frac{U_l(k', k'') k''^2 w_{k''}}{E(k) - E(k'')}. \quad (111)$$

If the k' index is allowed to span the same discrete indices as k'' , then the above matrix equation can be solved, and $R_l(k'', k)$ can be found. Observe, however, that k'' are transformed integration points that are not necessarily equal to the on-shell momentum, k . Since the main focus of the current work is elastic scattering, $R_l(k, k)$ is ultimately sought. To accomplish this, an additional point is added to the sum for the on-shell momentum, which is not an integration point: $k'' = k$ with weight $w_{k''} = 0$ for the $N + 1$ point. Consequently, the matrix equation becomes

$$\sum_{k''=1}^{N+1} \Lambda(k', k'') R_l(k'', k) = U_l(k', k), \quad (112)$$

and the solution of $R_l(k, k)$ can be found.

The number of partial waves needed for an acceptable tolerance of convergence is not known a priori. Partial waves were generated until $|T_l - U_l| \leq 10^{-4}\%$.

3.3 3D Lippmann-Schwinger

The numerical implementation of the LS3D method proceeds in the same manner as the PW method, but there are now two additional integration variables over azimuthal and polar angles. The azimuthal dependence only occurs in the potential and is integrated with 80 Gaussian quadrature points. As was seen with the PW method, the principal value integral over momenta is handled with Sloan's method [39], and an additional on-shell momentum is introduced such that $k'' = k$ with $w_{k''} = 0$ for the $N + 1$ Gaussian point; thus, equation (108) becomes,

$$\begin{aligned} T(k', x') = U(k', x') + \sum_{k''=1}^{N+1} \sum_{x''=1}^N \frac{\bar{U}(k', x', k'', x'') T(k'', x'') k''^2 w_{k''} w_{x''}}{E(k) - E(k'')} \\ - i\pi\mu^{\text{kin}} \sum_{k''=1}^{N+1} \sum_{x''=1}^N \bar{U}(k', x', k'', x'') T(k'', x'') k'' w_{x''} \delta_{k, k'}. \end{aligned} \quad (113)$$

Equation (113) can be written as a matrix equation,

$$\sum_{k''=1}^{N+1} \sum_{x''=1}^N \Lambda(k', x', k'', x'') T(k'', x'') = U(k', x'), \quad (114)$$

with

$$\begin{aligned} \Lambda(k', x', k'', x'') = \left[\delta_{k'', k'} \delta_{x'', x'} - \frac{\bar{U}(k', x', k'', x'') k''^2 w_{k''} w_{x''}}{E(k) - E(k'')} \right. \\ \left. + i\pi\mu^{\text{kin}} \bar{U}(k', x', k'', x'') k'' w_{x''} \delta_{k, k''} \right]. \end{aligned} \quad (115)$$

In order to solve the above matrix equation, k' is allowed to span the same discrete values of k'' ; likewise, x' uses the same discrete points as x'' .

The system of equations can be solved to obtain $T(k'', x'')$, where the solution is given for the on-shell and off-shell momenta at the Gaussian transformed angles, which are not evenly spaced. The transition matrix can be evaluated at any angle by substituting $T(k'', x'')$ into equation (113).

In order to solve equation (113), the summing indices are reduced to single indices,

$(k', x') \rightarrow i$ and $(k'', x'') \rightarrow j$, by using the following relations

$$i = x' + N(k' - 1) \quad (116)$$

and

$$j = x'' + N(k'' - 1), \quad (117)$$

where x' , x'' , k' , k'' represent discrete Gaussian transformed integration points (not continuous variables). N integration points have been used for the angular integration and $N + 1$ points have been used for the integration over momenta. Equation (114) reduces to the following complex system of linear equations:

$$\sum_{j=1}^{N(N+1)} \Lambda(i, j) T(j) = U(i). \quad (118)$$

Since the index i is allowed to vary over the same range as j , $N(N + 1)$ systems of equations must be solved (in contrast to $N + 1$ systems of equations for the PW method). Convergence of the total elastic cross sections was used to establish the number of Gaussian quadrature points used for integration. The number of Gaussian quadrature points for the LS3D solution method was increased to a maximum of $N = 44$ points such that the total elastic cross sections changed less than 1% for all reactions with energies up to 100 GeV/n.

3.4 Localized Contributions

It has been observed that the transition amplitude for reactions with large on-shell momenta—including high energy NA reactions and AA reactions at every energy—do not converge efficiently if the integration ranges of both momenta and polar angles are not restricted to regions that give significant contributions to the LS equation. The momenta which give non-zero contributions are estimated from the range of the optical potential and tend to be localized near the on-shell momentum, k .

The range of the potential is determined from the NN transition amplitude, nuclear matter densities, and kinematic factors. Consider a high energy collision of a projectile nucleon with a nucleus, such as ${}^4\text{He}$, which is modeled with a harmonic-well nuclear matter density (Gaussian). The transition amplitude and nuclear density are Gaussian functions of momentum transfer, $|q| = k^2 + k'^2 - 2kk' \cos(\theta)$. The greatest contributions occur when $k' \approx k$ at forward scattering angles. Therefore, the range of the potential is localized near the on-shell momentum and drops off quickly thereafter. At lower nucleon projectile energies, the on-shell momentum is smaller, and the range of the optical potential drops off more slowly. If one considers the collision of two light nuclei, then the range of the optical potential is further reduced because of the additional harmonic well density,

which is equivalent to multiplying with another q dependent Gaussian. Hence, even at low energies, the momenta that give non-zero optical potentials for AA reactions tend to be localized near the on-shell momentum.

The range of interaction may be estimated with a high degree of certainty using a forward scattering angle approach. The maximum range of the potential, R_{\max} , may be estimated at the forward scattering angle by moving outward from the on-shell momentum until the potential becomes effectively zero. As a measure of localization, a localization factor, μ_{loc} , is defined,

$$\mu_{\text{loc}} \equiv \frac{|k - R_{\max}|}{k}, \quad (119)$$

where k is the on-shell momentum. Small values are indicative of potentials that decay rapidly from the on-shell momentum. In the examples that follow, forward scattering has been used for the potentials, and the kinetic energy of the projectile in the laboratory frame has been used.

Fig. 4 shows the real part of the optical potential for a $p + {}^4\text{He}$ reaction at 100 MeV. At this energy, the NR and REL potentials are nearly equal, although there is a slight REL shift of the maximum toward a higher on-shell momentum. The localization factor for this reaction is $\mu_{\text{loc}} \approx 90\%$ and is an example of a potential that is not localized near the on-shell momentum.

In contrast to the low energy NA reaction, a $p + {}^4\text{He}$ reaction at 100 GeV is shown in Fig. 5. There is a significant shift in the REL on-shell momentum as compared to the NR k . It is also obvious that the maximum magnitude of the potential at k is reduced in the REL case. The momenta are highly localized for this reaction with a localization factor of $\mu_{\text{loc}} \leq 5\%$.

Figs. 6 and 7 show the real part of the optical potential for ${}^4\text{He} + {}^{20}\text{Ne}$ reactions at 100 MeV/n and 500 MeV/n. At 100 MeV/n, the localization factor is $\mu_{\text{loc}} \approx 22\%$, which is more localized than the NA reaction at the same energy. When the energy is increased to 500 MeV/n, the localization factor is reduced to $\mu_{\text{loc}} \approx 10\%$. This trend shows that the momenta become more localized near the on-shell momenta as the energy is increased. In addition, localization of momenta near k occurs at lower energies per nucleon for AA reactions than for NA reactions.

Figs. 8-11 illustrate the localization of momenta for equal mass systems. The real part of the optical potential is shown for low and high energy ${}^4\text{He} + {}^4\text{He}$ reactions in Figs. 8 and 9. Similar results are shown for ${}^{12}\text{C} + {}^{12}\text{C}$ reactions in Figs. 10 and 11. As expected, there is a slight difference between the NR and REL potentials at low energy. Differences become more obvious as the maximum of the potential decreases with increasing energy. There is no relativistic shift of the on-shell momentum due to kinematics for equal mass systems. In each case, the potential dies off rapidly from the on-shell momentum, and localization of momentum near k is clearly observed.

A small percentage ($10^{-8} \%$) of the maximum value of the elastic scattering optical

potential is used to estimate the range of the potential, R_{\max} , and the range of momenta (δ_R) from the on-shell value that give non-zero contributions to the LS equation, which the authors define as $\delta_R \equiv R_{\max} - k$. If $k - \delta_R > 0$, then the limits of integration are changed: $k'' \rightarrow [k - \delta_R, k + \delta_R]$. Note that the pole occurs at $k'' = k$, but if the integration is handled with Sloan's method [39], then the principal value singularity is removed because the pole is placed at the center of an even number of Gaussian quadrature points. When $k - \delta_R \leq 0$, the integration proceeds in the usual way: $[0, 2k]$ and $[2k, \infty)$.

High energy reactions tend to be forward scattering, so it is important to carefully specify the angular integration range such that convergence can be achieved efficiently. The elastic scattering optical potential was used to estimate the maximum range of the polar integration angle, θ_{\max} , and was used for all reactions presented in this document.

3.5 Equal Mass Kinematics

There are several kinematic factors that may change according to the kinematics selection: the on-shell momentum, k ; the elementary NN on-shell momentum, k_{elm} ; the elementary (NN) reduced mass, μ_{elm} ; the factor that transfers the transition amplitude to the scattering amplitude, $k(dk/dE)$; and the propagator. The relativistic (REL) on-shell momentum reduces to the non-relativistic (NR) on-shell momentum for equal mass systems; that is, $k^{\text{REL}} = k^{\text{NR}} = \sqrt{(mT_{\text{Lab}})/2}$, where m is the mass of the projectile or target, and T_{Lab} is kinetic energy of the projectile in the lab frame. Likewise, it follows that $k_{\text{elm}}^{\text{NR}} = k_{\text{elm}}^{\text{REL}}$.

To examine the effect of kinematics for equal mass systems, the LS equation is written as an infinite series,

$$T = V + VG_0^+T = V + VG_0^+V + VG_0^+VG_0^+V + \dots \quad (120)$$

Using completeness of over momenta, the matrix element of the transition amplitude may be written,

$$\begin{aligned} \langle \mathbf{k}' | T | \mathbf{k} \rangle = & \langle \mathbf{k}' | V | \mathbf{k} \rangle + \int \langle \mathbf{k}' | V | \mathbf{k}_1 \rangle \langle \mathbf{k}_1 | G_0^+ | \mathbf{k}_2 \rangle \langle \mathbf{k}_2 | V | \mathbf{k} \rangle d\mathbf{k}_1 d\mathbf{k}_2 \\ & + \int \langle \mathbf{k}' | V | \mathbf{k}_1 \rangle \langle \mathbf{k}_1 | G_0^+ | \mathbf{k}_2 \rangle \langle \mathbf{k}_2 | V | \mathbf{k}_3 \rangle \langle \mathbf{k}_3 | G_0^+ | \mathbf{k}_4 \rangle \langle \mathbf{k}_4 | V | \mathbf{k} \rangle d\mathbf{k}_1 d\mathbf{k}_2 d\mathbf{k}_3 d\mathbf{k}_4 + \dots \end{aligned} \quad (121)$$

After operating with the propagator, $\langle \mathbf{k}_i | G_0^+ | \mathbf{k}_j \rangle = G_0^+(k, k_i) \delta(\mathbf{k}_i - \mathbf{k}_j)$, the transition amplitude becomes,

$$\begin{aligned} \langle \mathbf{k}' | T | \mathbf{k} \rangle = & \langle \mathbf{k}' | V | \mathbf{k} \rangle + \int \langle \mathbf{k}' | V | \mathbf{k}_1 \rangle G_0^+(k, k_1) \langle \mathbf{k}_1 | V | \mathbf{k} \rangle d\mathbf{k}_1 \\ & + \int \langle \mathbf{k}' | V | \mathbf{k}_1 \rangle G_0^+(k, k_1) \langle \mathbf{k}_1 | V | \mathbf{k}_2 \rangle G_0^+(k, k_2) \langle \mathbf{k}_2 | V | \mathbf{k} \rangle d\mathbf{k}_1 d\mathbf{k}_2 + \dots, \end{aligned} \quad (122)$$

where the momenta have been relabeled for clarity.

The only kinematic factors that appear in the potential are k_{elm} and μ_{elm} , but, as previously stated, the elementary on-shell momenta are equivalent for NR and REL kinematics. Next, the scattering amplitude is obtained from the transition matrix, but only those factors that may lead to kinematic differences between the REL and NR scattering amplitudes are stated explicitly:

$$f(\theta) \propto k \frac{dk}{dE} \left[\sum_{n=1}^{\infty} \frac{1}{\mu_{\text{elm}}^n} \prod_{i=1}^{n-1} \frac{1}{[E(k) - E(k_i)]} \right], \quad (123)$$

where the momenta integration variables are k_i and the integration symbols have been suppressed. The NR scattering amplitude is expressed as

$$f^{\text{NR}}(\theta) \propto \sum_{n=1}^{\infty} 2^{n-1} A^n \prod_{i=1}^{n-1} \frac{1}{[k^2 - k_i^2]}, \quad (124)$$

and the REL scattering amplitude is

$$f^{\text{REL}}(\theta) \propto \sum_{n=1}^{\infty} A^n \prod_{i=1}^{n-1} \frac{[1 + h(k_i, k)]}{[k^2 - k_i^2]}, \quad (125)$$

where

$$h(k_i, k) = \sqrt{\frac{k_i^2 + m^2}{k^2 + m^2}}, \quad (126)$$

and A is the number of nucleons in the projectile or target. It can now be seen that, for equal mass systems, the REL scattering amplitude reduces to the NR amplitude when

$$h(k_i, k) \rightarrow 1. \quad (127)$$

For cases in which $k_i \approx k$, this condition is satisfied.

To illustrate the effect of the kinematics, the first couple of terms of the scattering amplitude are examined,

$$f^{\text{NR}}(\theta) \propto A + \frac{2A^2}{k^2 - k_i^2} + \dots \quad (128)$$

and

$$f^{\text{REL}}(\theta) \propto A + \frac{A^2[1 + h(k_i, k)]}{k^2 - k_i^2} + \dots \quad (129)$$

The relevant terms for comparison are

$$f_1 \equiv \frac{2}{k^2 - k''^2} \quad (130)$$

and

$$f_2 \equiv \frac{[1 + h(k'', k)]}{k^2 - k''^2}, \quad (131)$$

where k'' represents the integration variable.

The kinematic functions, f_1 and f_2 , for a ${}^4\text{He} + {}^4\text{He}$ reaction at $T_{\text{Lab}} = 3.3$ GeV/n ($k \approx 5$ GeV) are shown in Figs. 12-14. In Fig. 12, it appears that f_1 and f_2 are identical for all integration values, k'' . However, upon closer inspection in Fig. 13, differences are more clearly seen when k'' is farthest from the on-shell momentum. In Fig. 14, the black line shows the ratio f_2/f_1 , and the intersecting red, dashed lines show that the two functions are identical at the on-shell momentum. Fig. 12 clearly shows that the greatest contribution occurs at the pole. Similar results are shown in Figs. 15-17 for a ${}^{56}\text{Fe} + {}^{56}\text{Fe}$ reaction at $T_{\text{Lab}} = 100$ GeV/n.

In this section, it has been demonstrated that the relevant kinematic factors lead to NR and REL scattering amplitudes which are equal at the on-shell momentum for equal mass systems. Although differences between the scattering amplitudes can be observed when integration momenta are farthest away from the on-shell momentum, the greatest contributions occur near the pole. As a result, very little difference between scattering amplitudes will be observed for equal mass systems.

4 Results

In the results that follow, each model uses the same set of fundamental parameterizations for nuclear matter densities and the NN transition amplitude. Harmonic well and two-parameter Fermi (Wood-Saxon) nuclear charge data are taken from references [13, 14] and are normalized to matter densities as described in reference [5]. When data are not available for the two-parameter Fermi densities, a nuclear droplet model [40] is used for parameter estimates. Nuclei are assumed to be near the beta stability curve. The NN transition amplitude used in the current work is described in Appendix A and depends on parameterizations of the NN cross sections, slope parameter, and real to imaginary ratio of the transition amplitude. The NN cross sections are taken from reference [41]. Parameterizations of the slope parameters and real to imaginary ratios of the data in reference [42] are given in Appendix B.

In Figs. 18-24, NA and AA elastic differential cross sections are shown at energies that are relevant to space radiation applications, including $p + {}^{16}\text{O}$, $p + {}^{56}\text{Fe}$, ${}^4\text{He} + {}^4\text{He}$, ${}^4\text{He} + {}^{16}\text{O}$, ${}^{12}\text{C} + {}^{56}\text{Fe}$, ${}^{20}\text{Ne} + {}^{20}\text{Ne}$, and ${}^{56}\text{Fe} + {}^{56}\text{Fe}$ reactions at lab projectile kinetic energies of 150, 500, 1000, and 20,000 MeV/n. The projectile energy of 150 MeV/n represents the

lower bound on model applicability. Results are indicated non-relativistic by (NR) and relativistic by (REL). LS3D (REL) results are given as a solid red line; a dashed, black line is used for eikonal results, denoted (Eik); a green square represents the PW (NR) results; a solid blue circle indicates LS3D (NR) results; and a violet asterisk is for PW (REL) results. Note that the Coulomb interaction has not been included in this analysis.

Excellent agreement between PW and LS3D results are seen in Figs. 18-21 for each kinematic selection for energies greater than 150 MeV. The $p + {}^{16}\text{O}$ and $p + {}^{56}\text{Fe}$ reactions at 150 MeV/n in Figs. 18 and 19 show slight disagreements between NR PW and LS3D codes and eikonal results. This is likely the result of the forward scattering approximation used in the eikonal method, since very light projectiles may deviate from forward scattering at low energy. The slight disagreement between the eikonal and NR PW and LS3D codes is not observed for the heavier nuclei in Figs. 20 and 21, where the small angle scattering approximation is more appropriate.

The next obvious feature is that of the relativistic shift observed in Figs. 18-21. The magnitude of the differential cross section is larger at smaller angles as compared to the NR cases. The effect is more pronounced at higher energies, as expected, but is also driven by projectile and target mass differences. A comparison of Figs. 18 and 20 shows that the relativistic effect is more pronounced for the $p + {}^{16}\text{O}$ reaction, which has larger mass difference than the ${}^4\text{He} + {}^{16}\text{O}$ system. Ultimately, the relativistic effects can be tracked back to kinematic differences in the relative on-shell momentum.

Elastic scattering for equal mass systems is depicted in Figs. 22-24. Fig. 22 shows the elastic differential cross section for ${}^4\text{He} + {}^4\text{He}$. At the lowest energies, the eikonal model appears to accurately describe the scattering at small angles, but begins to deviate from the other models at higher angles. The most obvious difference between Fig. 22 and Figs. 18-21 is that there is no shift in the differential cross section at higher energies in Fig. 22. Moreover, there is no relativistic shift observed in Figs. 23 and 24 for the ${}^{20}\text{Ne} + {}^{20}\text{Ne}$ and ${}^{56}\text{Fe} + {}^{56}\text{Fe}$ reactions. It was demonstrated in section 3.5 that the REL scattering amplitude is equal to the NR amplitude at the on-shell momentum for equal mass systems and that the largest contributions near the pole. Therefore, there is no differential cross section shift associated with the REL kinematics for equal mass systems.

All of the reactions presented in Figs. 18-24 have been extended to 100 GeV/n. The results at this energy are consistent with the 20 GeV/n reactions and have not been shown here, although, as expected, there is a larger shift in the differential cross section for unequal mass systems.

As an example of the LS3D method and illustration of the relativistic shift, comparisons to experimental data [43–46] are performed. Fig. 25 shows the elastic differential cross sections of the following reactions: (a) $p + {}^{32}\text{S}$ at $T_{\text{Lab}} = 1$ GeV [43] (b) $p + {}^{40}\text{Ca}$ at $T_{\text{Lab}} = 500$ MeV [44] (c) $p + {}^{58}\text{Ni}$ at $T_{\text{Lab}} = 1$ GeV [45] and (d) ${}^4\text{He} + {}^{40}\text{Ca}$ at $T_{\text{Lab}} = 347$ MeV/n [46]. NR results are indicated as a solid red line, and REL results are indicated with a solid blue line. In each case, there is better agreement with experiment when relativistic kinematics are used. Since the fundamental parameterizations are based on

small-angle scattering data, the results are in better agreement with the measured differential cross section data at forward scattering angles. Also note that spin-dependence and medium effects have not been included, which may account for differences between the model and the experimental data in Fig. 25 (d).

5 Conclusions

The eikonal, PW, and LS3D methods have been compared for NA and AA reactions for reactions relevant for space radiation applications. Numerical convergence of the eikonal method is readily achieved when the formulas presented herein are used for light nuclei ($A \leq 16$) and the momentum-space representation of the optical potential is used for heavier nuclei. The LS formalism has an advantage over the eikonal method in that relativistic kinematics are easily included. The PW solution method is numerically unstable for reactions that have large on-shell momenta, including both high energy reactions and relatively low energy AA reactions, due to the highly oscillatory Legendre polynomials needed for convergence of these systems. To circumvent this difficulty, the 3D solution method was implemented. Convergence of the LS3D equation can be achieved quickly after identifying the integration range for momenta and polar angles that give non-zero contributions to the LS equation. This numerical method is also useful for obtaining convergence for the partial wave analysis; however, numerical instability still exists because of the Legendre polynomial oscillations.

It was shown that the NR PW and NR LS3D methods agree with the eikonal method, except at very low energies for projectile nucleons, where the eikonal method is not well-suited. As the lab energy is increased, relativistic effects are seen as a shift in differential cross section resonances toward higher magnitudes and lower angles. There was no observed relativistic shift of the differential cross section for equal mass systems. It was shown in section 3.5 that the NR and REL on-shell momentum are equal for equal mass systems and that the largest contributions to the LS equation occur near the pole, k .

Based on the results presented herein, it is recommended that the LS3D method be used for high energy NA and AA reactions at all energies because of its rapid numerical convergence and stability. Extensive comparisons between models and experimental data are underway. The results of that research and a verification and validation analysis of the models will be elucidated in a future manuscript.

6 Appendix A

NN transition amplitude and nuclear matter densities

In this appendix, the position space representation and Fourier transforms of the NN transition amplitude and nuclear matter densities are given. Usually, harmonic-well

nuclear matter densities are used for $A \leq 16$, and Wood-Saxon matter densities are used for $A > 16$ [5, 16]. The harmonic-well matter density in position space is [5]

$$\rho^{\text{HW}}(r) = (\alpha + \beta r^2) \exp \left[\frac{-r^2}{4s^2} \right], \quad (132)$$

where

$$\alpha = \frac{\rho_0^{\text{HW}} a^3}{8s^3} \left[1 + \frac{3\gamma}{2} - \frac{3\gamma a^2}{8s^2} \right] \quad (133)$$

and

$$\beta = \frac{\rho_0^{\text{HW}} a^3}{8s^3} \frac{\gamma a^2}{16s^4}, \quad (134)$$

The normalization factor is

$$\rho_0^{\text{HW}} = \frac{1}{\pi^{3/2} a^3 [1 + \frac{3}{2}\gamma]}, \quad (135)$$

where γ and a are parameters given in references [13, 14], $s^2 = a^2/4 - r_p^2/6$, and r_p is the proton radius [5, 16]. The Fourier transform of the harmonic-well nuclear matter density is given by [5]

$$\rho^{\text{HW}}(q) = \rho_0^{\text{HW}} \pi^{3/2} a^3 \left[\left(1 + \frac{3}{2}\gamma \right) - \frac{a^2 \gamma}{4} q^2 \right] e^{-q^2 s^2}. \quad (136)$$

The Wood-Saxon nuclear matter density is given as [5]

$$\rho^{\text{WS}}(r) = \frac{\rho_0^{\text{WS}}}{1 + e^{\frac{r-R}{c_A}}}, \quad (137)$$

where the normalization is

$$\rho_0^{\text{WS}} = \frac{3}{4\pi} \left[\frac{1}{R^3 + \pi^2 c_A^2 R} \right]. \quad (138)$$

R is the half density radius, and c_A is related to the surface diffuseness, c , by [5]

$$c_A = \frac{2r_p}{\sqrt{3}} \ln \left[\left(\frac{3\beta - 1}{3 - \beta} \right) \right]^{-1} \quad (139)$$

and

$$\beta = \exp \left[\frac{r_p}{c\sqrt{3}} \right], \quad (140)$$

where r_p is the proton radius. The parameters, R and c , are given in references [13, 14].

The Fourier transform of the Wood-Saxon matter density is [12]

$$\rho^{\text{WS}}(q) = \frac{4\pi}{q} \rho_0^{\text{WS}} \phi(q), \quad (141)$$

where

$$\phi(q) = \pi c_A R \left[\frac{-\cos(qR)}{\sinh(qc_A\pi)} + \frac{\pi c_A}{R} \frac{\sin(qR) \coth(qc_A\pi)}{\sinh(qc_A\pi)} - \frac{2c_A}{\pi R} \sum_{n=1}^{\infty} \frac{(-1)^n n q c_A}{[(qc_A)^2 + n^2]^2} \right]. \quad (142)$$

The NN transition amplitude is [5]

$$t_{\text{NN}}(r) = \tau \exp \left[\frac{-r^2}{2B(e_{\text{NN}})} \right] \quad (143)$$

with

$$\tau = -\sqrt{\frac{e_{\text{NN}}}{m}} \frac{\sigma(e_{\text{NN}})}{[2\pi B(e_{\text{NN}})]^{3/2}} [\kappa(e_{\text{NN}}) + i], \quad (144)$$

where e_{NN} is the kinetic energy of the NN system in the CM frame, m_p is the proton mass, $B(e_{\text{NN}})$ is the slope parameter, $\sigma(e_{\text{NN}})$ is the NN cross section, and $\kappa(e_{\text{NN}})$ is the real to imaginary ratio of the NN cross section.

The Fourier transform of the NN transition amplitude is given as [5]

$$t_{\text{NN}}(q) = \frac{-1}{(2\pi)^2} \frac{1}{\mu} \frac{k\sigma(e_{\text{NN}})}{4\pi} [\kappa(e_{\text{NN}}) + i] e^{-B(e_{\text{NN}})q^2/2}, \quad (145)$$

where μ is the reduced mass of the NN system, and k is the relative momentum in the NN CM frame.

7 Appendix B

Real to imaginary ratios and slope parameters for the proton-proton (pp) and proton-neutron (pn) cross sections are given in this section and are parameterized to the data listed in reference [42]. The parameterizations are a function of proton kinetic energy in the lab frame, ϵ , with energy in units of GeV.

The pp real to imaginary ratio is

$$\kappa_{\text{pp}} = \begin{cases} c_0 + c_1\epsilon, & \text{for } 0 \leq \epsilon \leq 0.2 \text{ GeV} \\ \frac{a+c\epsilon+e\epsilon^2+g\epsilon^3}{1+b\epsilon+d\epsilon^2+f\epsilon^3}, & \text{for } \epsilon < 0.2 \leq 100 \text{ GeV}, \end{cases} \quad (146)$$

where $c_0 = 1.0736$, $c_1 = -0.8370 \text{ GeV}^{-1}$, and $a = 1.3204$, $b = 1.0713 \text{ GeV}^{-1}$, $c = -0.9240 \text{ GeV}^{-1}$, $d = 1.0478 \text{ GeV}^{-2}$, $e = -0.3279 \text{ GeV}^{-2}$, $f = 0.01601 \text{ GeV}^{-3}$, and $g = 0.0025 \text{ GeV}^{-3}$.

The np real to imaginary ratio is given by

$$\kappa_{np} = \begin{cases} c_0 + c_1\epsilon, & \text{for } 0 \leq \epsilon \leq 0.15 \text{ GeV} \\ \frac{a+c\epsilon}{1+b\epsilon+d\epsilon^2}, & \text{for } \epsilon < 0.15 \leq 100 \text{ GeV}, \end{cases} \quad (147)$$

where $c_0 = 0.7763$, $c_1 = 2.2886 \text{ GeV}^{-1}$, and $a = 3.2411 \times 10^8$, $b = 1.1305 \times 10^9 \text{ GeV}^{-1}$, $c = -7.8409 \times 10^8 \text{ GeV}^{-1}$, $d = 8.0467 \times 10^7 \text{ GeV}^{-2}$.

The slope parameter for the pp reactions is

$$B_{pp} = \frac{a + c\epsilon + e\epsilon^2}{1 + b\epsilon + d\epsilon^2 + f\epsilon^3} \quad (148)$$

where $a = 0.4665 \text{ fm}^2$, $b = 0.4319 \text{ GeV}^{-1}$, $c = 0.2897 \text{ fm}^2 \text{ GeV}^{-1}$, $d = 5.5596 \times 10^{-3} \text{ GeV}^{-2}$, $e = 4.5448 \times 10^{-3} \text{ fm}^2 \text{ GeV}^{-2}$, and $f = 3.2662 \times 10^{-6} \text{ GeV}^{-3}$. For the np reactions, the slope parameter is

$$B_{np} = \frac{a + c\epsilon + e\epsilon^2 + g\epsilon^3}{1 + b\epsilon + d\epsilon^2 + f\epsilon^3}, \quad (149)$$

where $a = 0.4622 \text{ fm}^2$, $b = -0.1776 \text{ GeV}^{-1}$, $c = -0.0139 \times 10^{-3} \text{ fm}^2 \text{ GeV}^{-1}$, $d = 0.0207 \text{ GeV}^{-2}$, $e = -6.5369 \times 10^{-3} \text{ fm}^2 \text{ GeV}^{-2}$, $f = 6.9016 \times 10^{-3} \text{ GeV}^{-3}$, $g = 4.9074 \times 10^{-3} \text{ fm}^2 \text{ GeV}^{-3}$.

8 Appendix C

Kinematics

The relative on-shell momentum in the CM frame is needed as input for the LS equation. This appendix describes the NR and REL kinematics for reactions of the form,

$$A + B \rightarrow C + D, \quad (150)$$

where the relative momentum is written as a function of the kinetic energy of the projectile in the laboratory frame.

8.1 Non-relativistic Kinematics

With NR kinematics, the relative momentum may be expressed as

$$\mathcal{P}_i = \frac{m_B \mathbf{p}_A - m_A \mathbf{p}_B}{m_A + m_B}, \quad (151)$$

where m_A is the mass of the projectile, \mathbf{p}_A is the momentum of the projectile, m_B is the mass of the target, \mathbf{p}_B is the momentum of the target. $\mathcal{P}_i = \mathbf{p}_{A\text{CM}} = -\mathbf{p}_{B\text{CM}}$, where $\mathbf{p}_{i\text{CM}}$ is the momentum of particle i in the CM frame. The momentum of particle B in the lab frame is $\mathbf{p}_{B\text{Lab}} = \mathbf{0}$, and the relative momentum can be written as

$$\mathcal{P}_i = \frac{m_B}{m_A + m_B} \mathbf{p}_{A\text{Lab}}, \quad (152)$$

where $\mathbf{p}_{A\text{Lab}}$ is the momentum of particle A in the lab frame. The kinetic energy available in the CM frame is

$$T_{\text{CM}} = \mathcal{P}_i^2 / 2\mu = T_{\text{Lab}} \left(\frac{m_B}{m_A + m_B} \right), \quad (153)$$

where $T_{\text{Lab}} = \mathbf{p}_{A\text{Lab}}^2 / 2m_A$ and $\mu = m_A m_B / (m_A + m_B)$. If the kinetic energy of the projectile in the lab frame is given, then the relative on-shell momentum may be obtained from

$$k \equiv |\mathcal{P}_i| = \sqrt{2\mu T_{\text{CM}}} = \sqrt{\frac{2\mu m_B T_{\text{Lab}}}{m_A + m_B}}. \quad (154)$$

8.2 Relativistic Kinematics

In this section, the relativistic momentum is expressed as a function of T_{Lab} . The four-momentum is denoted with a superscript, μ , to avoid confusion with previous discussions in this document. In the lab frame, the four-momenta of particles A and B are

$$p_{A\text{Lab}}^\mu = (E_{A\text{Lab}}, \mathbf{p}_{A\text{Lab}}) \quad \text{and} \quad p_{B\text{Lab}}^\mu = (m_B, \mathbf{0}), \quad (155)$$

and in the CM frame,

$$p_{A\text{CM}}^\mu = (E_{A\text{CM}}, \mathbf{p}_{A\text{CM}}) \quad \text{and} \quad p_{B\text{CM}}^\mu = (E_{B\text{CM}}, \mathbf{p}_{B\text{CM}}), \quad (156)$$

where $E_{i\text{Lab}}$ is the relativistic energy for particle i in the lab frame, $E_{i\text{CM}}$ is the relativistic energy for particle i in the CM frame, $\mathbf{p}_{i\text{Lab}}$ is the three-momentum for particle i in the lab frame, and $\mathbf{p}_{i\text{CM}}$ is the three-momentum for particle i in the CM frame.

The Mandelstam variable, s , is an invariant defined by the four-vector's length, $s = (p_A^\mu + p_B^\mu)^2$. In the CM frame, $s = (E_A + E_B, \mathbf{0})^2$, and the total energy is \sqrt{s} . In the lab frame,

$$s = (p_{A\text{Lab}}^\mu + p_{B\text{Lab}}^\mu)^2 = m_A^2 + m_B^2 + 2m_B E_{A\text{Lab}}. \quad (157)$$

The kinetic energy is found by subtracting the rest mass from the total energy, $T_{A\text{Lab}} = E_{A\text{Lab}} - m_A$, so

$$s = (m_A + m_B)^2 + 2m_B T_{A\text{Lab}}. \quad (158)$$

The Mandelstam variable can be used to express the total energy as a function of the relative three-momentum by using the CM frame,

$$s = (E_A + E_B)^2 = \left(\sqrt{\mathcal{P}_i^2 + m_A^2} + \sqrt{\mathcal{P}_i^2 + m_B^2} \right)^2, \quad (159)$$

where $\mathcal{P}_i = \mathbf{p}_{A_{\text{CM}}} = -\mathbf{p}_{B_{\text{CM}}}$. After performing the square and regrouping terms,

$$|\mathcal{P}_i| = \frac{1}{2\sqrt{s}} \sqrt{[s - (m_A^2 + m_B^2)]^2 - 4m_A^2 m_B^2}. \quad (160)$$

Substituting equation (157) into equation (160) leads to the final result for the relative momentum,

$$k \equiv |\mathcal{P}_i| = \frac{m_B}{\sqrt{s}} \sqrt{T_{A_{\text{Lab}}} [T_{A_{\text{Lab}}} + 2m_A]}. \quad (161)$$

References

- [1] M. Ackermann et al., *Science* **339**, 807 (2013).
- [2] E. R. Benton and E. V. Benton, *Nucl. Instr. Meth. B* **184**, 255 (2001).
- [3] T. C. Slaba, S. R. Blattnig, and F. F. Badavi, *J. Comput. Phys.* **229**, 9397 (2010).
- [4] T. C. Slaba, S. R. Blattnig, M. S. Cloudsley, S. A. Walker, and F. F. Badavi, *Adv. Space Res.* **46**, 800 (2010).
- [5] J. W. Wilson, L. W. Townsend, W. Schimmerling, G. S. Khandelwal, F. Khan, J. E. Nealy, F. A. Cucinotta, L. C. Simonsen, J. L. Shinn, and J. W. Norbury, *Transport methods and interactions for space radiations*, NASA Reference Publication 1257 (1991).
- [6] J. A. Simpson, *Ann. Rev. Nucl. Part. Sci.* **33**, 323 (1983).
- [7] C. J. Joachain, *Quantum Collision Theory* (American Elsevier, New York, 1983).
- [8] H. Feshbach, *Ann. Phys.* **5**, 357 (1958).
- [9] H. Feshbach, *Ann. Phys.* **19**, 287 (1962).
- [10] A. Picklesimer, P. C. Tandy, R. Thaler, and D. Wolfe, *Phys. Rev. C* **30**, 1861 (1984).
- [11] A. Picklesimer, P. C. Tandy, R. Thaler, and D. Wolfe, *Phys. Rev. C* **29**, 1582 (1984).
- [12] D. H. Wolfe, Ph.D. thesis, Kent State University (1983).

- [13] C. W. De Jager, H. De Vries, and C. De Vries, *Atom. Data Nucl. Data* **14**, 479 (1974).
- [14] H. De Vries, C. W. De Jager, and C. De Vries, *Atom. Data Nucl. Data* **36**, 495 (1987).
- [15] M. L. Miller, K. Reygers, S. J. Sanders, and P. Steinberg, *Annu. Rev. Nucl. Part. Sci.* **57**, 205 (2007).
- [16] L. W. Townsend, H. B. Bidasaria, and J. W. Wilson, *Can. J. Phys.* **61**, 867 (1983).
- [17] J. W. Wilson, *Phys. Lett. B* **52**, 419 (1974).
- [18] J. W. Wilson and L. W. Townsend, *Can. J. Phys.* **59**, 1569 (1981).
- [19] L. W. Townsend, J. W. Wilson, and H. B. Bidasaria, *Can. J. Phys.* **60**, 1514 (1982).
- [20] L. W. Townsend, *Can. J. Phys.* **61**, 93 (1983).
- [21] C. M. Werneth, K. M. Maung, L. R. Mead, and S. R. Blattnig, *Nucl. Instr. Meth. B* **308**, 40 (2013).
- [22] C. Elster, J. H. Thomas, and W. Glockle, *arXiv:9708017v1 [nucl-th]* (1997).
- [23] I. Fachruddin, C. Elster, and W. Glockle, *Phys. Rev. C* **62**, 044002 (2000).
- [24] M. Rodriguez-Gallardo, A. Deltuva, E. Cravo, R. Crespo, and A. C. Fonseca, *Phys. Rev. C* **78**, 034602 (2008).
- [25] S. Veerasamy, C. Elster, and W. N. Polyzou, *Few Body Systems* **54**, 2207 (2013).
- [26] H. Liu, C. Elster, and W. Glockle, *Phys. Rev. C* **72**, 054003 (2005).
- [27] K. M. Maung, J. W. Norbury, and T. Coleman, *J. Phys. G: Nucl. Part. Phys.* **34**, 1861 (2007).
- [28] K. M. Watson, *Phys. Rev.* **89**, 575 (1953).
- [29] C. M. Werneth and K. M. Maung, *Can. J. Phys.* **91**, 424 (2013).
- [30] C. Elster, S. P. Weppner, and C. R. Chinn, *Phys. Rev. C* **56**, 2080 (1997).
- [31] D. J. Ernst and D. L. Weiss, *Phys. Rev. C* **26**, 605 (1982).
- [32] D. J. Ernst, G. A. Miller, and D. L. Weiss, *Phys. Rev. C* **27**, 2733 (1983).
- [33] C. Möller, *K. Dan. Vidensk. Selsk. Mat.-Fys. Medd.* **23**, 1 (1945).

- [34] R. J. Glauber, *Lectures in Theoretical Physics* (Interscience Publishers Inc., New York, 1959).
- [35] H. B. Bidasaria and L. W. Townsend, *Analytic Optical Potentials for Nucleon-Nucleus and Nucleus-Nucleus Collisions Involving Light and Medium Nuclei*, NASA Technical Memorandum 83224 (1982).
- [36] L. W. Townsend and H. B. Bidasaria, *Analytic Determinations of Single-Folding Optical Potentials*, NASA Technical Memorandum 84611 (1983).
- [37] R. H. Landau, *Quantum Mechanics II: A Second Course in Quantum Theory* (John Wiley & Sons Inc., New York, 1996).
- [38] L. S. Rodberg and R. M. Thaler, *Introduction to Quantum Theory of Scattering* (Adademic Press, New York, 1967).
- [39] I. H. Sloan, J. Comput. Phys. **3**, 332 (1968).
- [40] W. D. Meyers and W. J. Swiatecki, Ann. Phys. **84**, 186 (1974).
- [41] J. W. Norbury, *Total Nucleon-Nucleon Cross Section*, NASA Technical Publication 2008-215116.
- [42] J. W. Wilson and C. M. Costner, *Nucleon and heavy-ion total and absorption cross section for selected nuclei*, NASA Technical Note D-8107 (1975).
- [43] G. D. Alkhazov, G. M. Amalsky, S. L. Belostotsky, A. A. Vorobyov, O. A. Domchenkov, and Y. V. Dotsenko, Phys. Lett. B **42**, 121 (1972).
- [44] G. W. Hoffmann et al., Phys. Rev. Lett. **47**, 1436 (1981).
- [45] R. M. Lombard, G. D. Alkhazov, and O. A. Domchenkov, Nucl. Phys. A **360**, 233 (1981).
- [46] G. D. Alkhazov et al., Nucl. Phys. A **280**, 365 (1977).

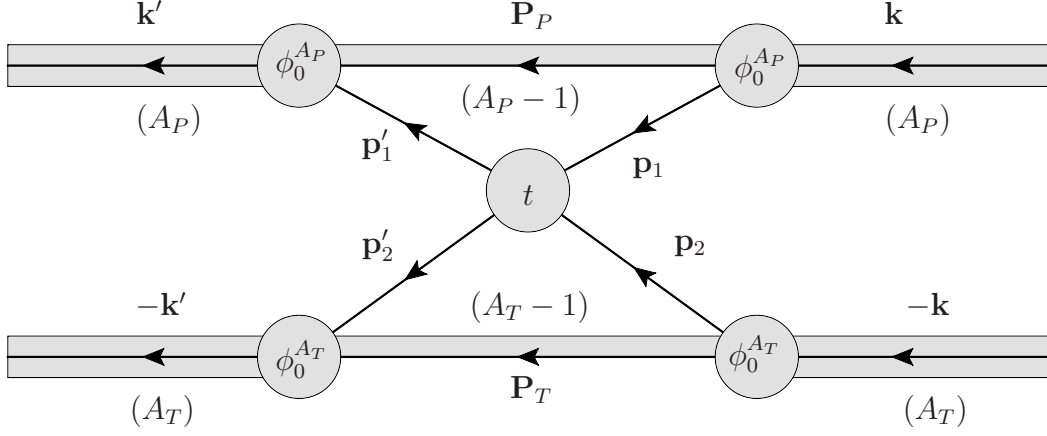


Figure 1: Transition amplitude for AA scattering in the AA CM frame. \mathbf{k} (\mathbf{k}') is the initial(final) momentum of the projectile nucleus in the AA CM frame. $-\mathbf{k}$ ($-\mathbf{k}'$) is the initial(final) momentum of the target nucleus in the AA CM frame. The internal nucleon momenta are denoted \mathbf{p}_1 and \mathbf{p}_2 . \mathbf{P}_P and \mathbf{P}_T are the momenta of the core of the $A_P - 1$ virtual projectile and $A_T - 1$ virtual target nuclei, respectively. See text for explanation.

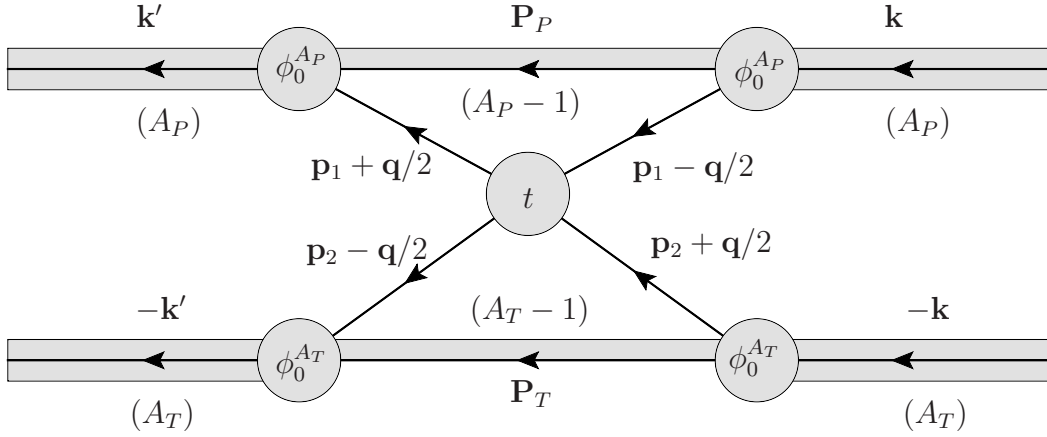


Figure 2: Optimum factorization for AA scattering in the AA CM frame. \mathbf{k} (\mathbf{k}') is the initial(final) momentum of the projectile nucleus in the AA CM frame. $-\mathbf{k}$ ($-\mathbf{k}'$) is the initial(final) momentum of the target nucleus in the AA CM frame. The internal nucleon momenta are denoted \mathbf{p}_1 and \mathbf{p}_2 . \mathbf{P}_P and \mathbf{P}_T are the momenta of the core of the $A_P - 1$ virtual projectile and $A_T - 1$ virtual target nuclei, respectively. \mathbf{q} is the momentum transfer for the AA system. See text for explanation.

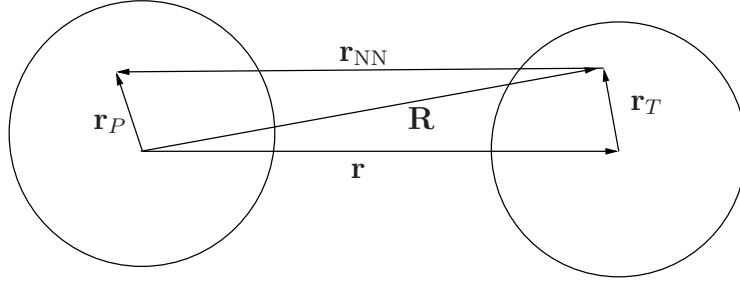


Figure 3: Illustration of the vectors used for the nucleus-nucleus optical potential. The distance from the center of the projectile nucleus to a nucleon in the projectile nucleus is \mathbf{r}_P . Likewise, \mathbf{r}_T is the distance from the center of the target nucleus to a nucleon in the target. The center to center distance between nuclei is \mathbf{r} , and \mathbf{r}_{NN} is the distance between a nucleon in the projectile to a nucleon in the target. $\mathbf{R} = \mathbf{r} + \mathbf{r}_T$ is the distance from the center of the projectile to a nucleon in the target.

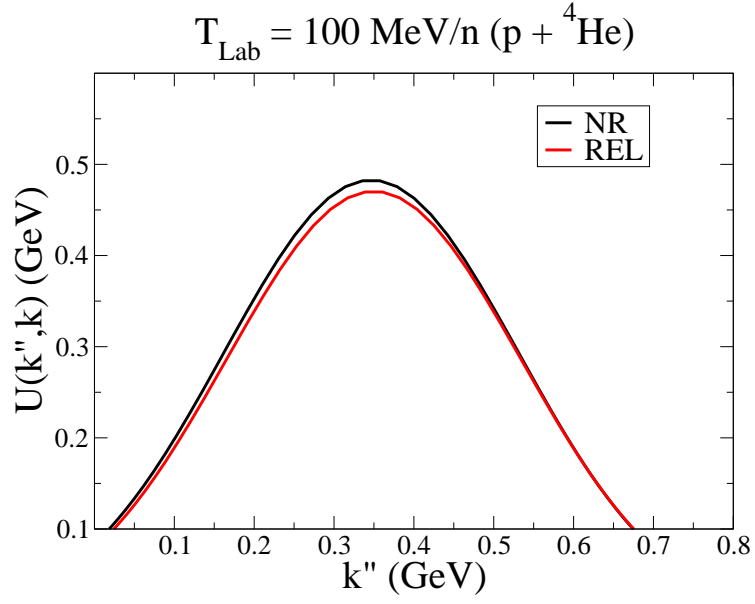


Figure 4: Real part of optical potential for a $p + ^4\text{He}$ reaction with $T_{\text{Lab}} = 100 \text{ MeV}$ (NR $k \approx 346 \text{ MeV}$ and REL $k \approx 349 \text{ MeV}$) at $\theta_{\text{CM}} = 0$.

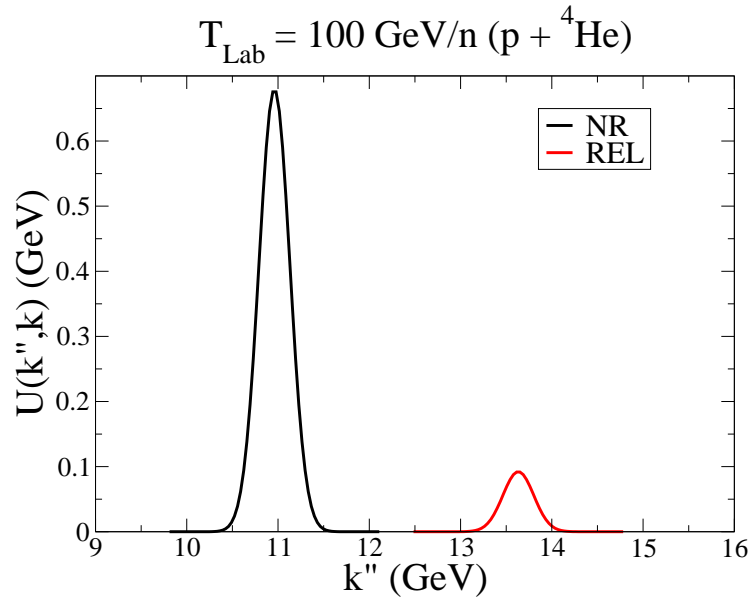


Figure 5: Real part of optical potential for a $T_{\text{Lab}} = 100 \text{ GeV}$ (NR $k \approx 10.96 \text{ GeV}$ and REL $k \approx 13.63 \text{ GeV}$) $p + ^4\text{He}$ reaction at $\theta_{\text{CM}} = 0$.

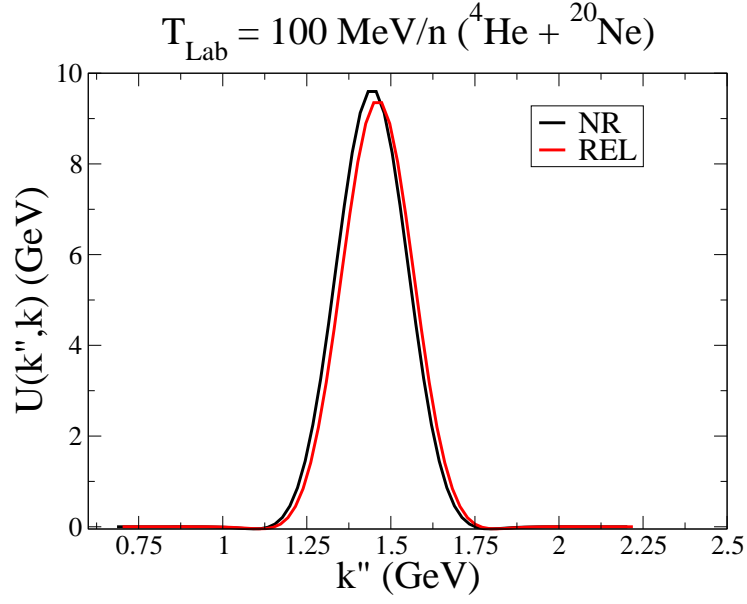


Figure 6: Real part of optical potential for a $T_{\text{Lab}} = 100 \text{ MeV/n}$ (NR $k \approx 1.44 \text{ GeV}$ and REL $k \approx 1.46 \text{ GeV}$) $^4\text{He} + ^{20}\text{Ne}$ reaction at $\theta_{\text{CM}} = 0$.

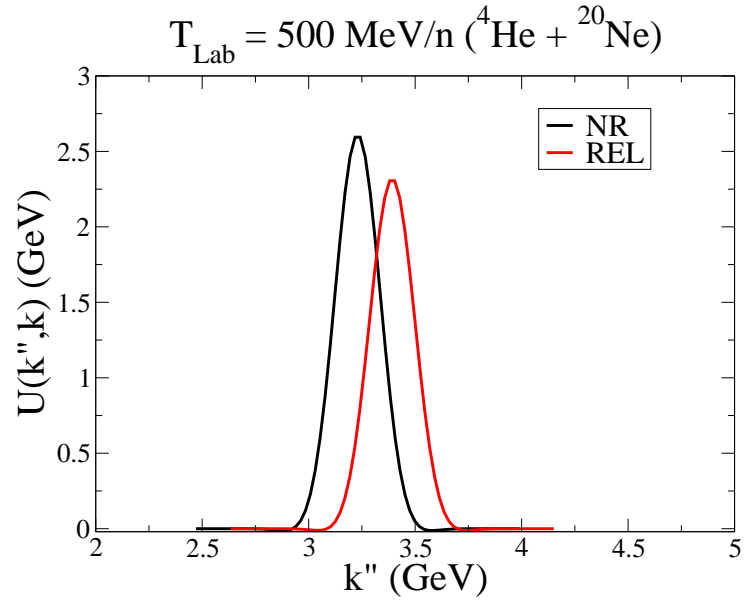


Figure 7: Real part of optical potential for a $T_{\text{Lab}} = 500 \text{ MeV/n}$ (NR $k \approx 3.23 \text{ GeV}$ and REL $k \approx 3.39 \text{ GeV}$) $^4\text{He} + ^{20}\text{Ne}$ reaction at $\theta_{\text{CM}} = 0$.

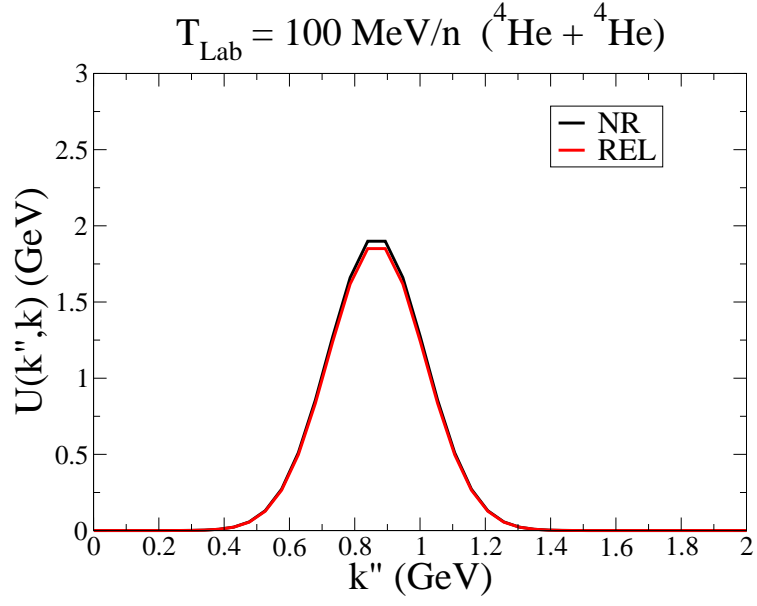


Figure 8: Real part of optical potential for a $T_{\text{Lab}} = 100 \text{ MeV/n}$ ($k \approx 0.87 \text{ GeV}$) $^4\text{He} + ^4\text{He}$ reaction at $\theta_{\text{CM}} = 0$.

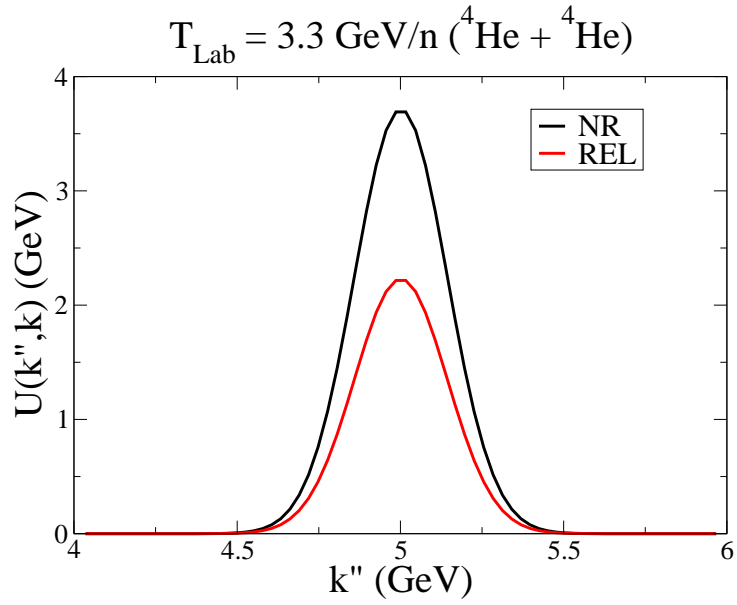


Figure 9: Real part of optical potential for a $^4\text{He} + ^4\text{He}$ reaction with $T_{\text{Lab}} = 3.3 \text{ GeV/n}$ ($k \approx 5 \text{ GeV}$) at $\theta_{\text{CM}} = 0$.

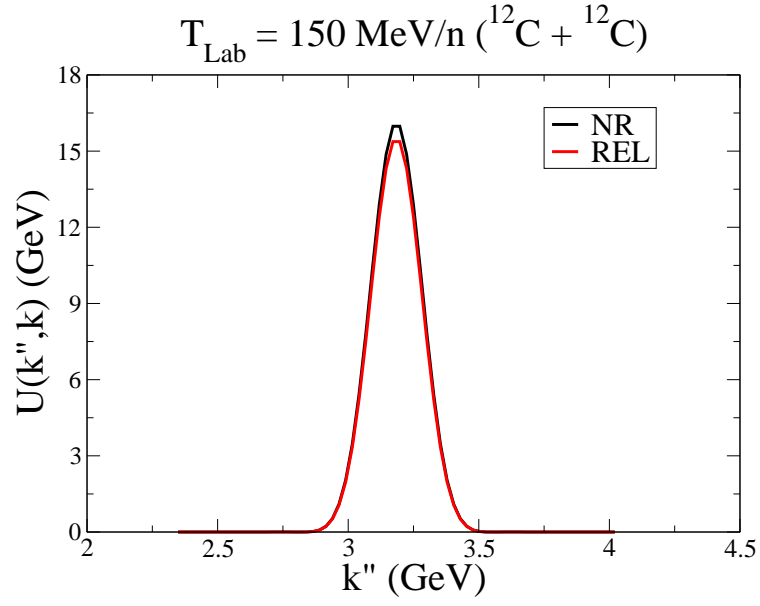


Figure 10: Real part of optical potential for a $^{12}\text{C} + ^{12}\text{C}$ reaction at 150 MeV/n ($k \approx 3.18$ GeV) with $\theta_{\text{CM}} = 0$.

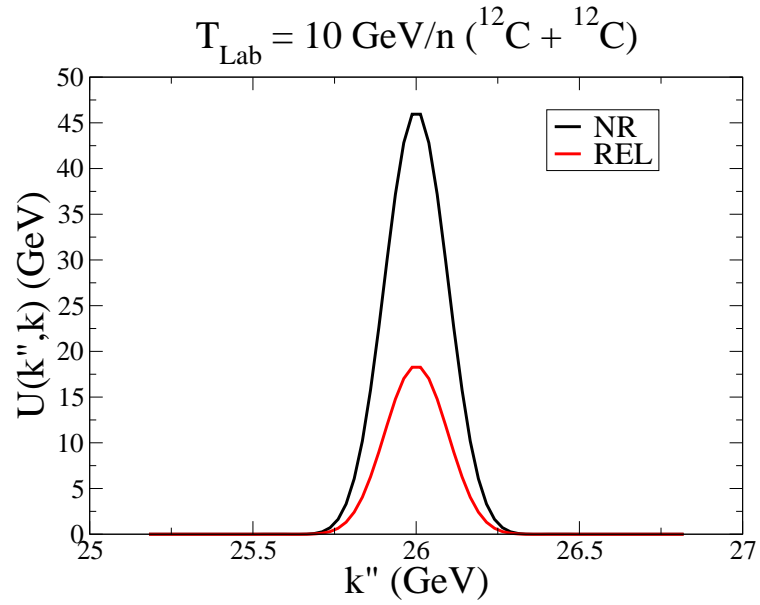


Figure 11: Real part of optical potential for a $^{12}\text{C} + ^{12}\text{C}$ reaction at 10 GeV/n ($k \approx 26$ GeV) with $\theta_{\text{CM}} = 0$.

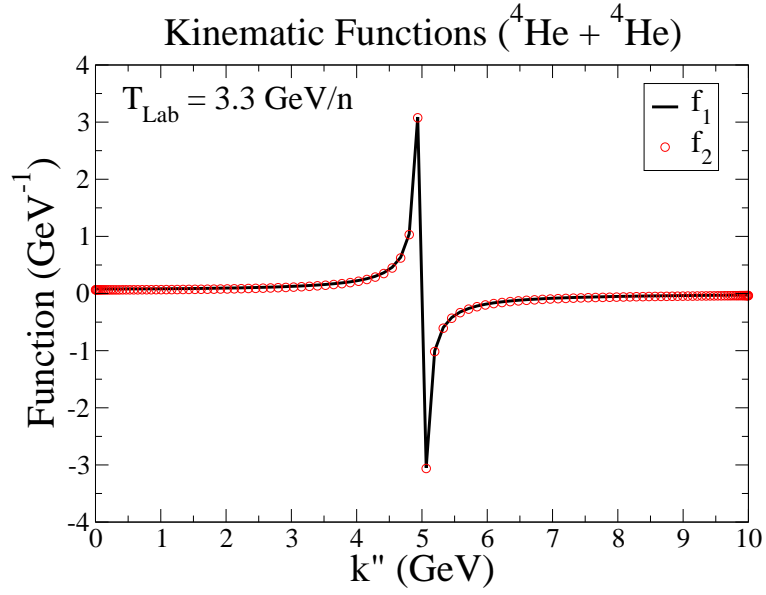


Figure 12: Kinematic functions, f_1 and f_2 , for a ${}^4\text{He} + {}^4\text{He}$ reaction at $T_{\text{Lab}} = 3.3 \text{ GeV/n}$ ($k \approx 5 \text{ GeV}$). The integration variable is denoted k'' .

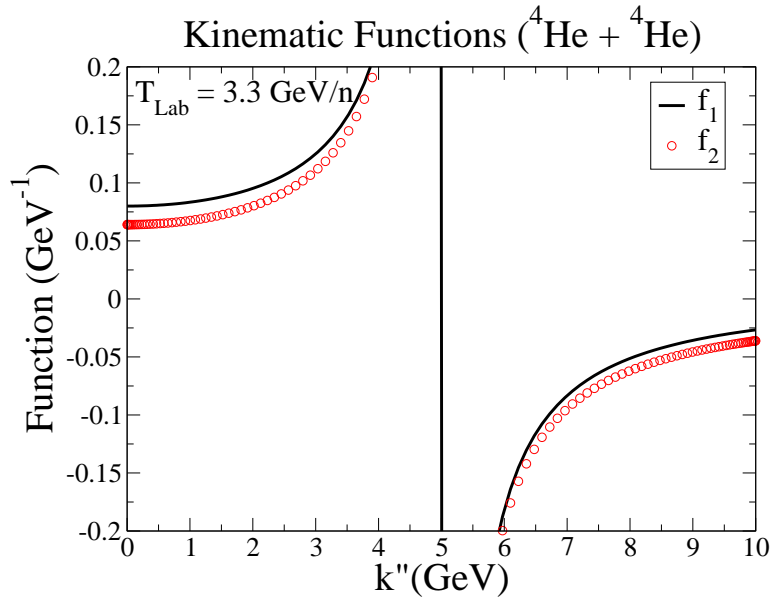


Figure 13: Alternate view of kinematic functions, f_1 and f_2 , for a ${}^4\text{He} + {}^4\text{He}$ reaction with on-shell momentum $k \approx 5 \text{ GeV}$. The integration variable is denoted k'' .

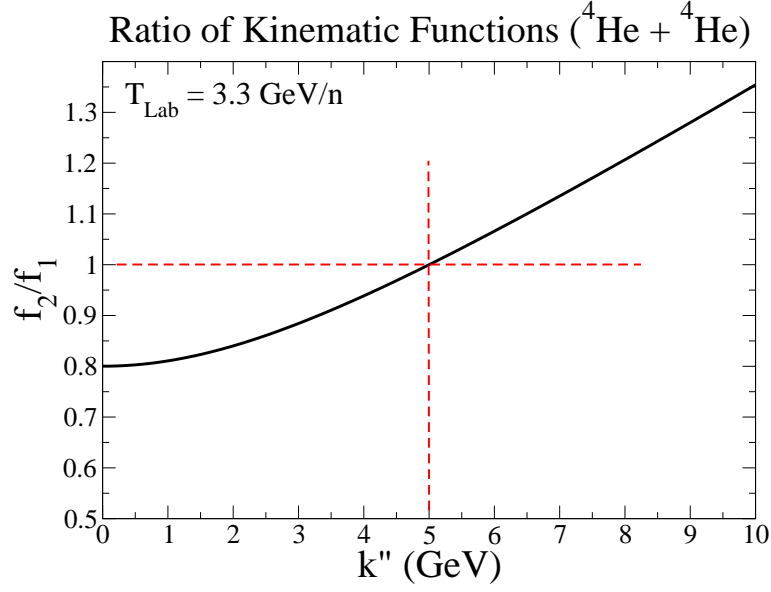


Figure 14: Ratio of kinematic functions, f_2/f_1 . The two functions are identical at the on-shell momentum, shown with intersecting red, dashed lines. The integration variable is denoted k'' .

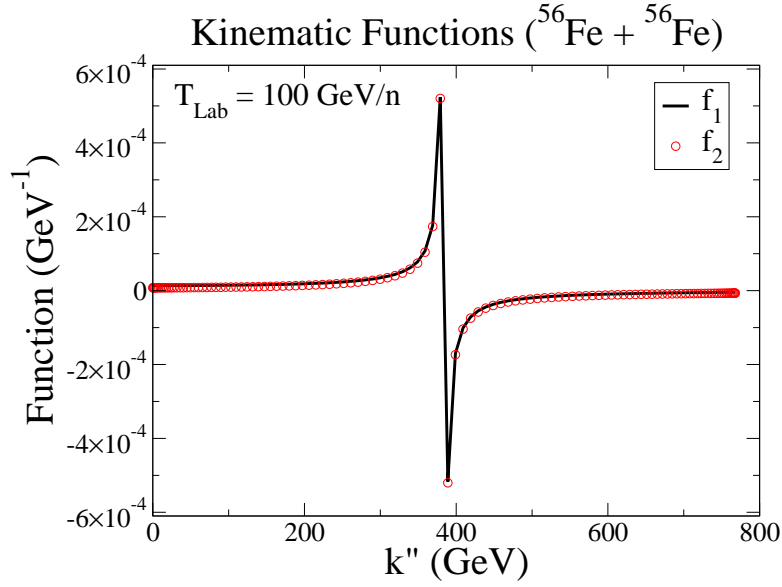


Figure 15: Kinematic functions, f_1 and f_2 , for a $^{56}\text{Fe} + ^{56}\text{Fe}$ reaction at $T_{\text{Lab}} = 100$ GeV/n ($k \approx 384$ GeV). The integration variable is denoted k'' .

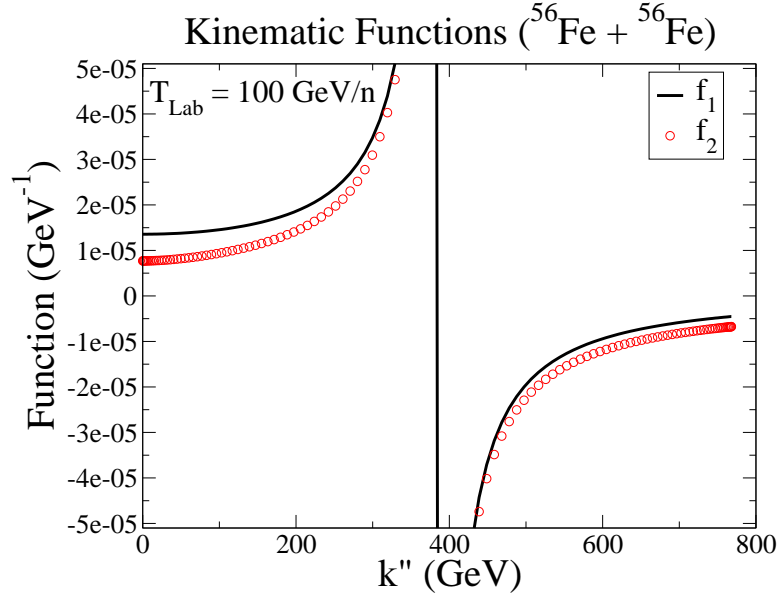


Figure 16: Alternate view of kinematic functions, f_1 and f_2 , for a $^{56}\text{Fe} + ^{56}\text{Fe}$ reaction with on-shell momentum $k \approx 384$ GeV. The integration variable is denoted k'' .

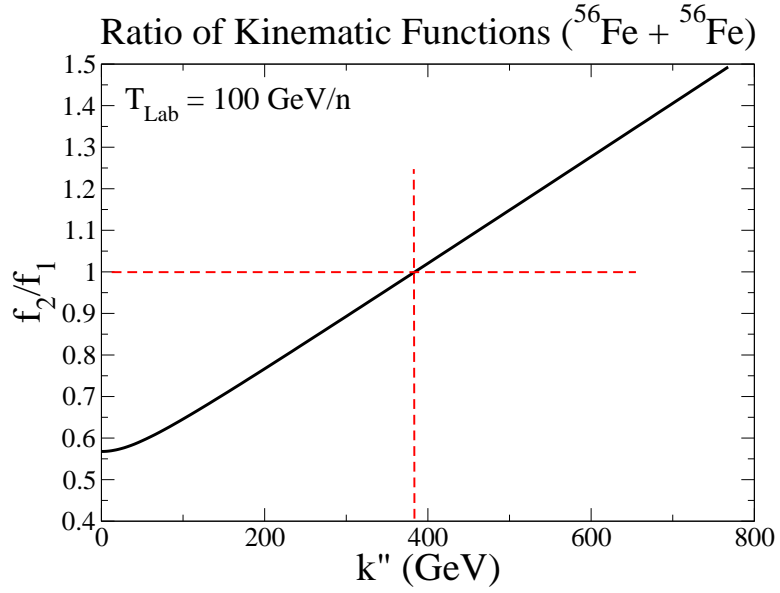


Figure 17: Ratio of kinematic functions, f_2/f_1 . The two functions are identical at the on-shell momentum, shown with intersecting red, dashed lines. The integration variable is denoted k'' .

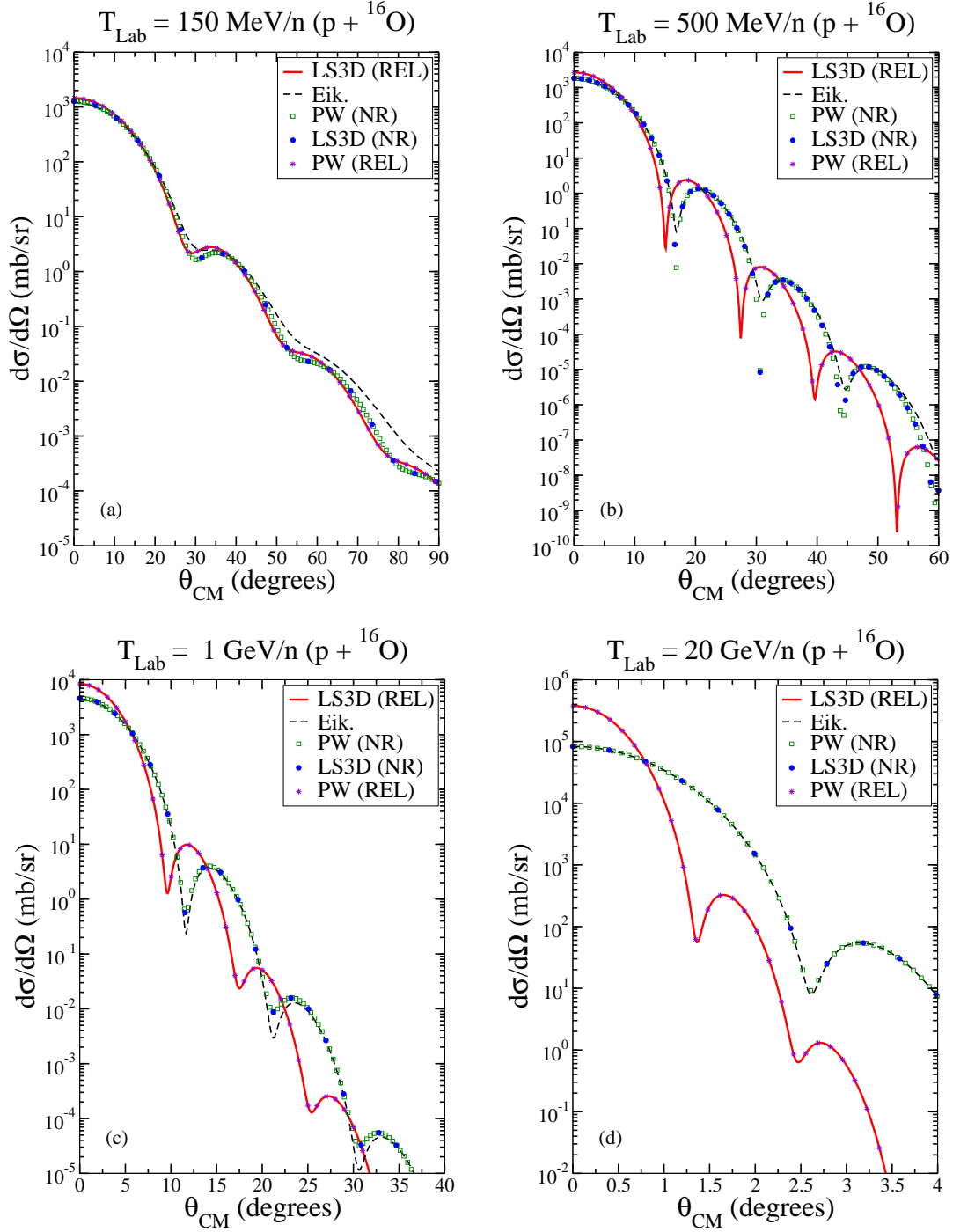


Figure 18: Elastic differential cross sections for $p + {}^{16}\text{O}$ reactions for projectile lab kinetic energies of 150, 500, 1000, 20000 MeV. Eik. represents eikonal, LS3D represents three-dimensional Lippmann-Schwinger, and PW represents partial wave. Non-relativistic results are denoted (NR) and relativistic results are denoted (REL).

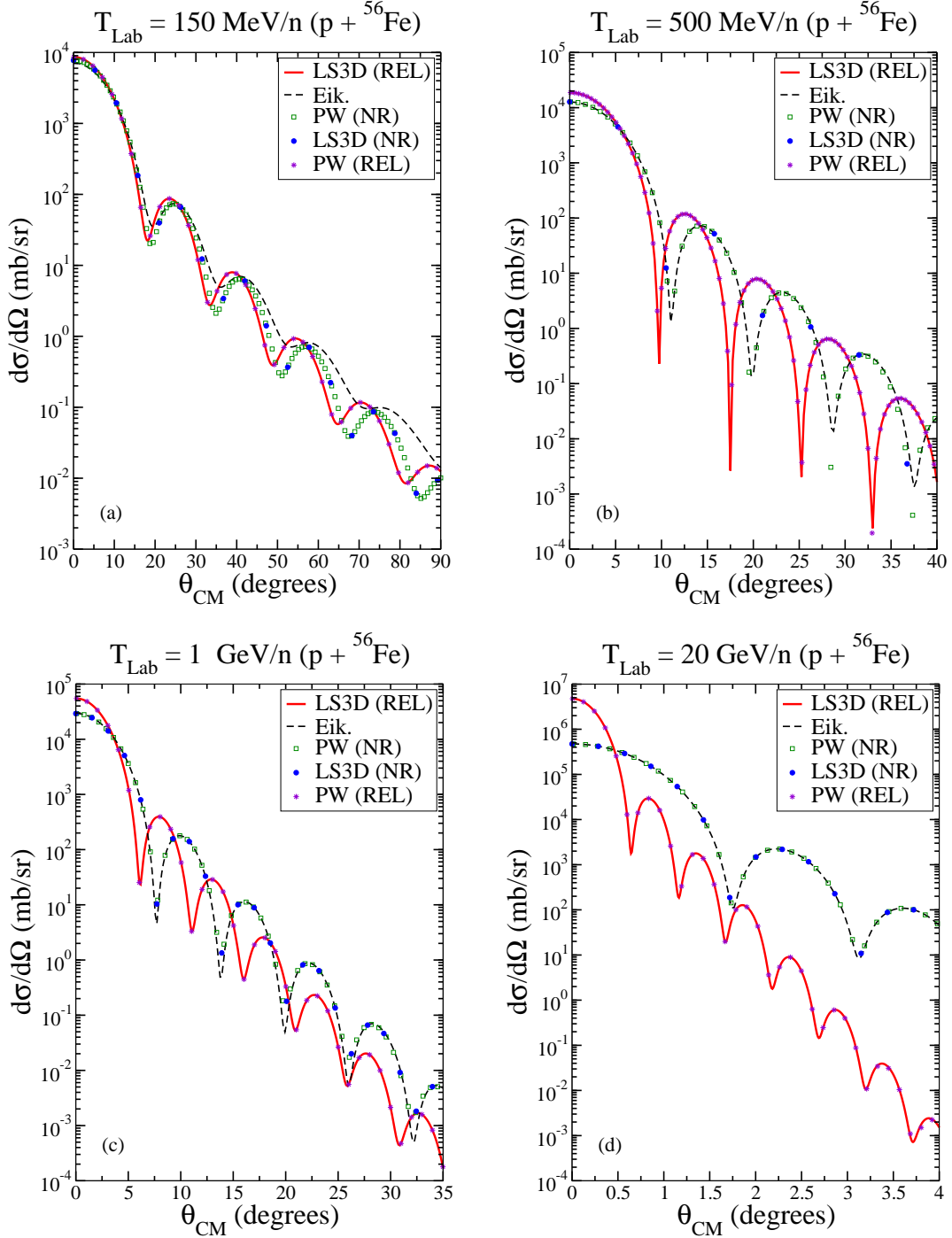


Figure 19: Elastic differential cross sections for $p + {}^{56}\text{Fe}$ reactions for projectile lab kinetic energies of 150, 500, 1000, 20000 MeV. Eik. represents eikonal, LS3D represents three-dimensional Lippmann-Schwinger, and PW represents partial wave. Non-relativistic results are denoted (NR) and relativistic results are denoted (REL).

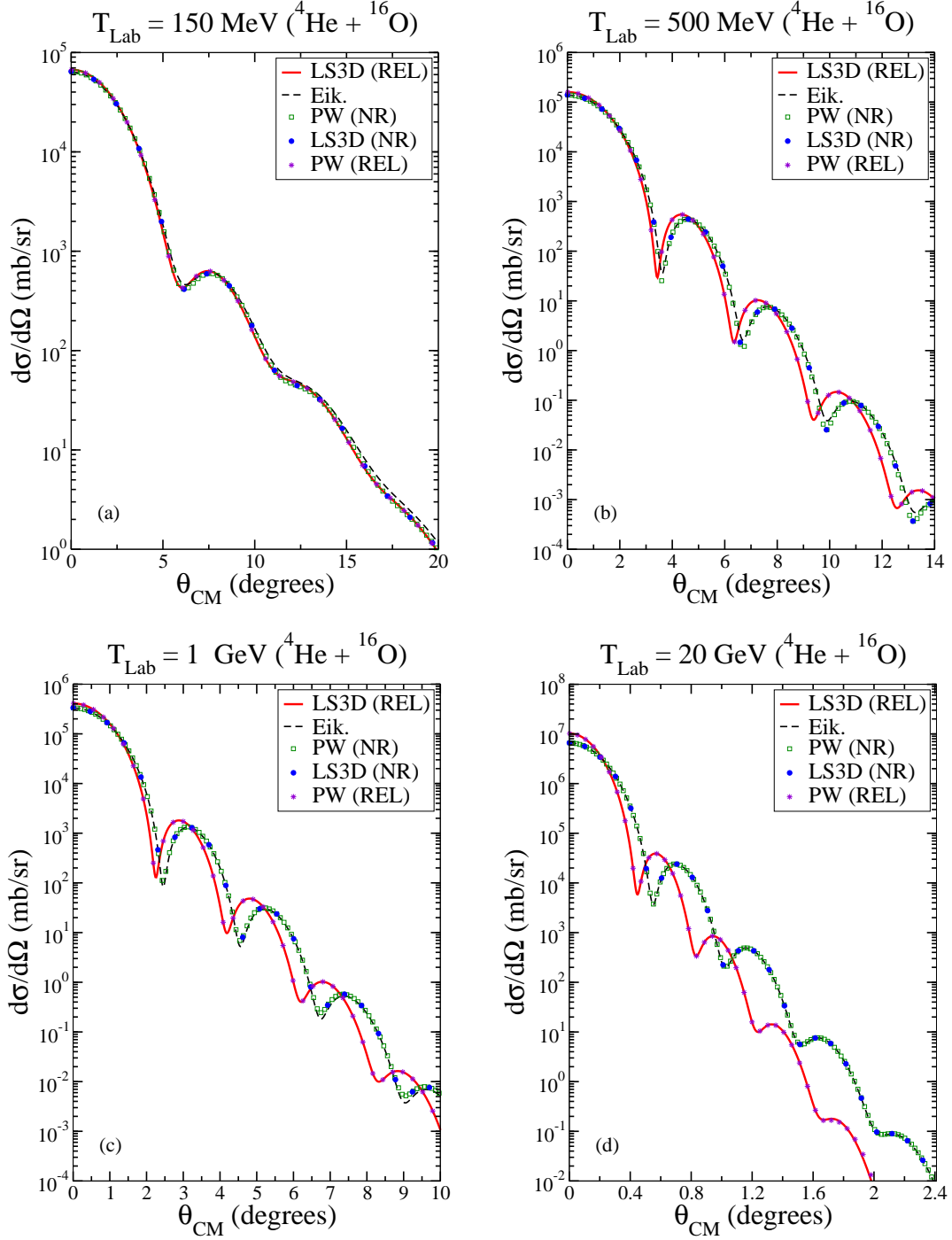


Figure 20: Elastic differential cross sections for $^4\text{He} + ^{16}\text{O}$ reactions for projectile lab kinetic energies of 150, 500, 1000, 20000 MeV/n. Eik. represents eikonal, LS3D represents three-dimensional Lippmann-Schwinger, and PW represents partial wave. Non-relativistic results are denoted (NR) and relativistic results are denoted (REL).

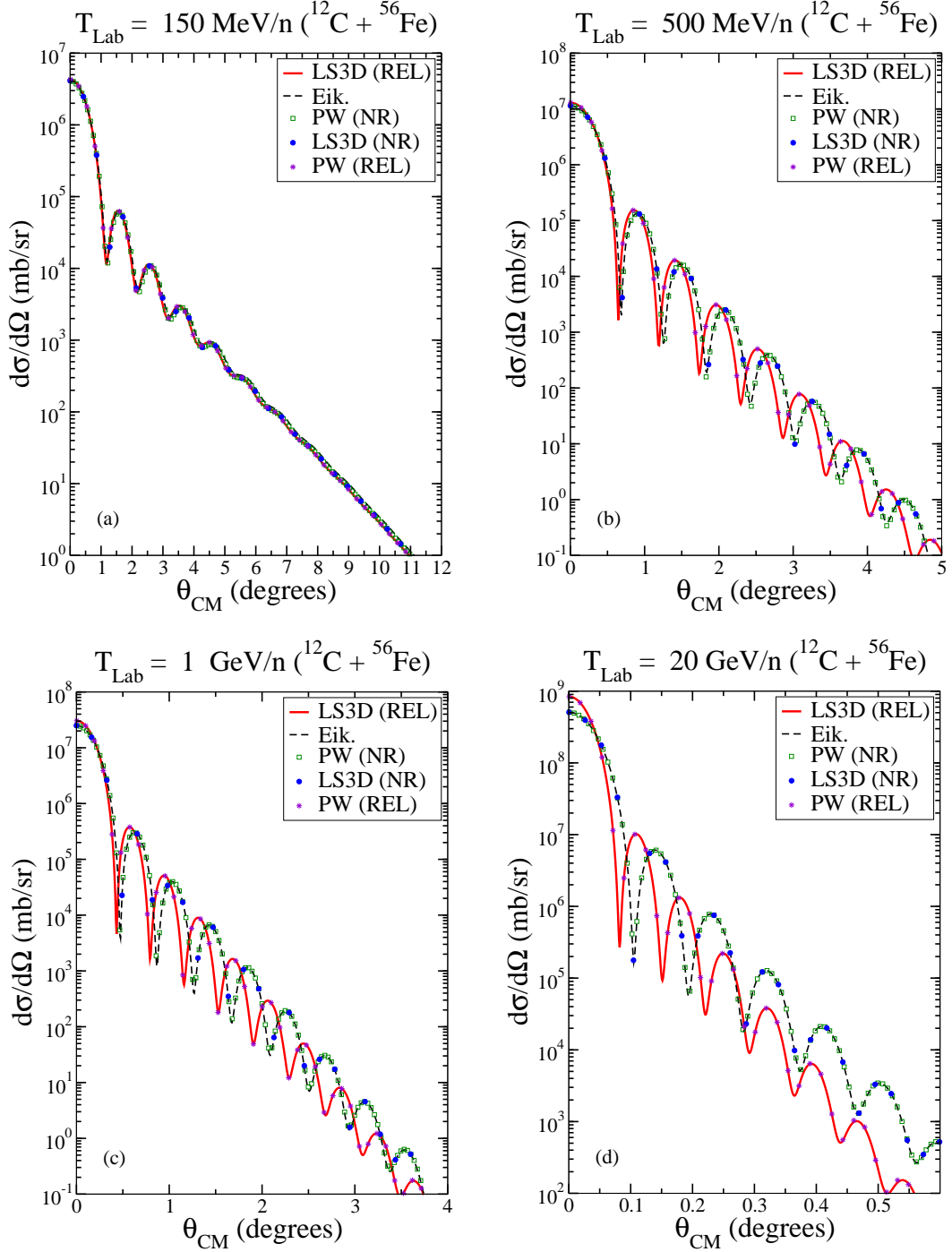


Figure 21: Elastic differential cross sections for $^{12}\text{C} + ^{56}\text{Fe}$ reactions for projectile lab kinetic energies of 150, 500, 1000, 20000 MeV/n. Eik. represents eikonal, LS3D represents three-dimensional Lippmann-Schwinger, and PW represents partial wave. Non-relativistic results are denoted (NR) and relativistic results are denoted (REL).

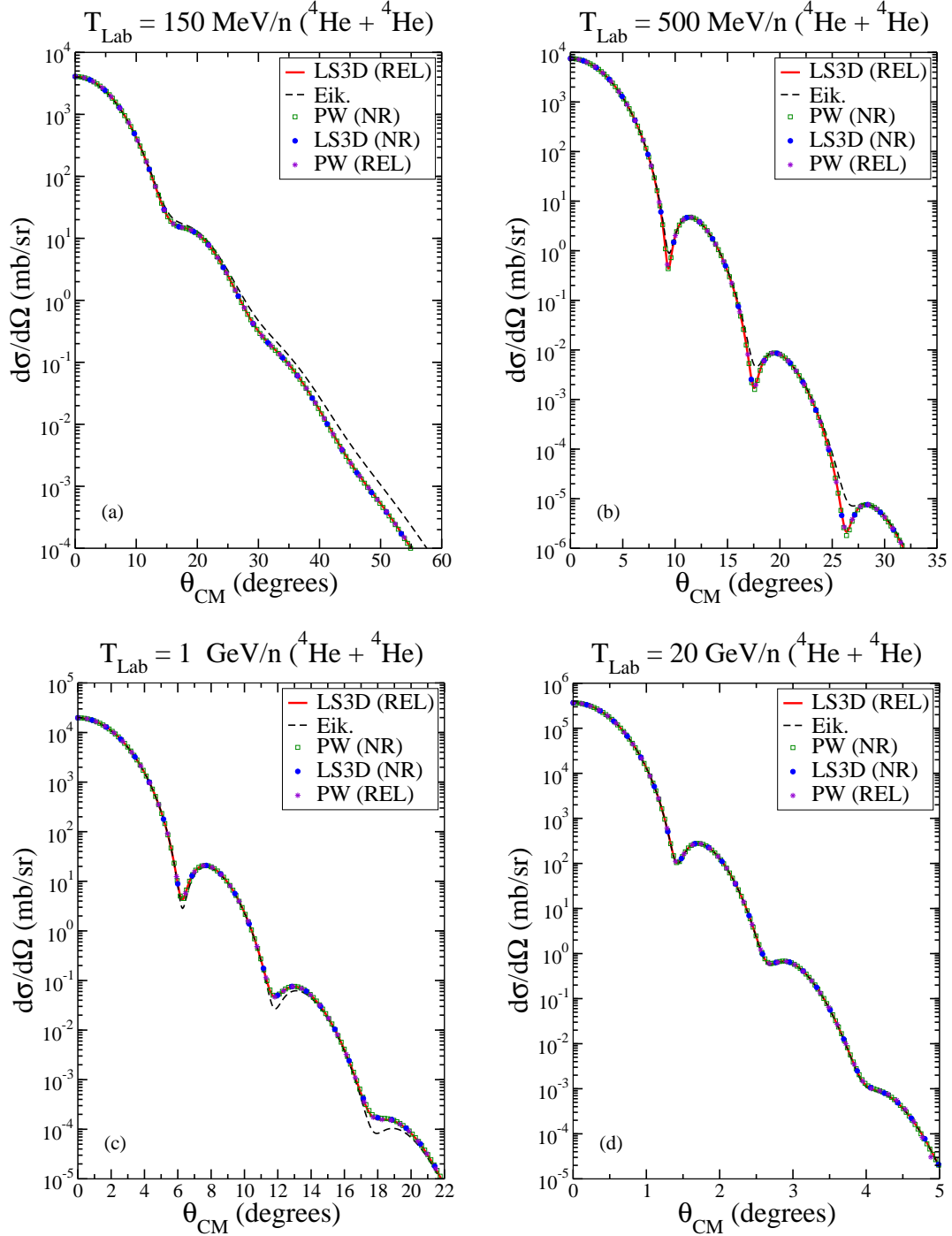


Figure 22: Elastic differential cross sections for ${}^4\text{He} + {}^4\text{He}$ reactions for projectile lab kinetic energies of 150, 500, 1000, 20000 MeV/n. Eik. represents eikonal, LS3D represents three-dimensional Lippmann-Schwinger, and PW represents partial wave. Non-relativistic results are denoted (NR) and relativistic results are denoted (REL).

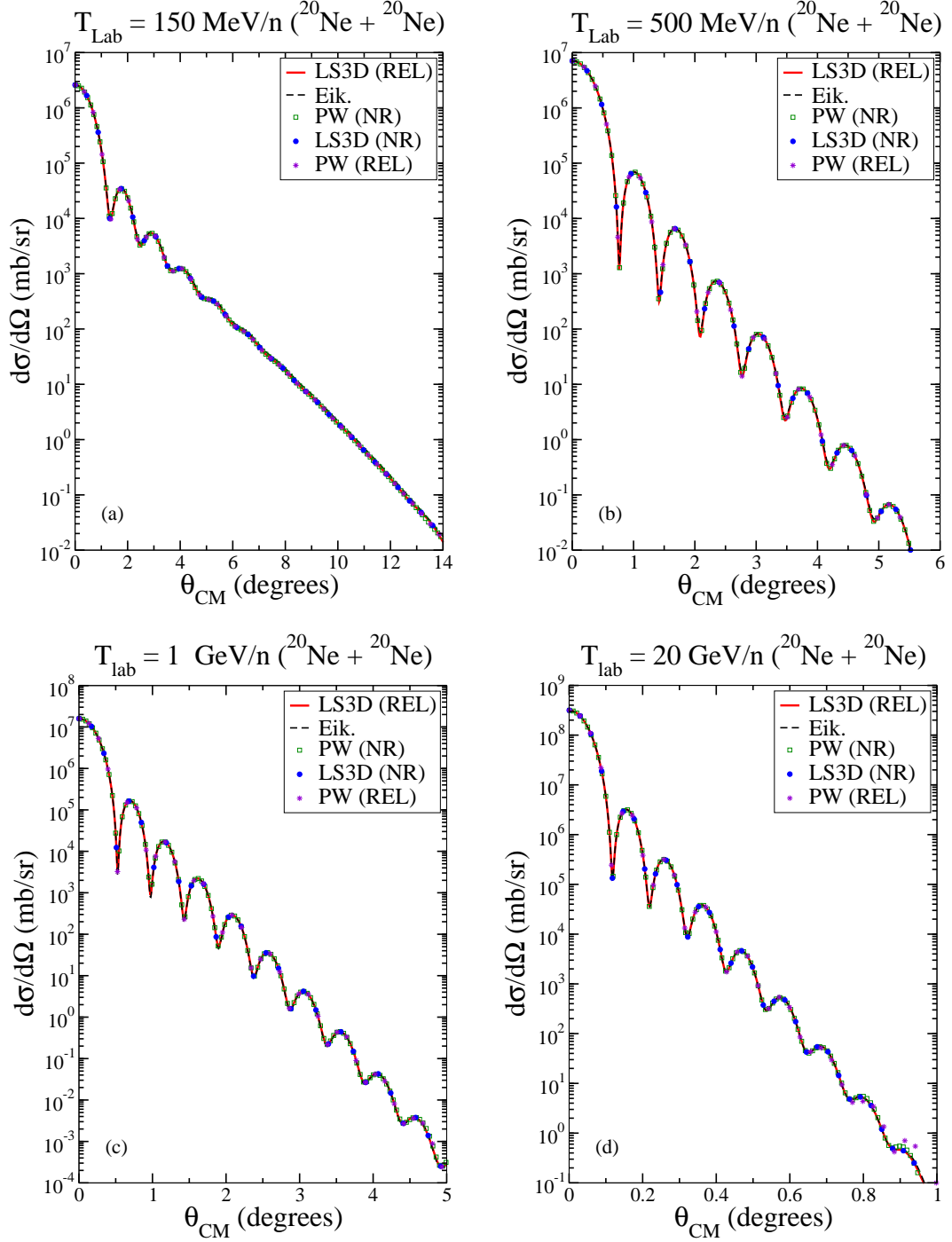


Figure 23: Elastic differential cross sections for $^{20}\text{Ne} + ^{20}\text{Ne}$ reactions for projectile lab kinetic energies of 150, 500, 1000, 20000 MeV/n. Eik. represents eikonal, LS3D represents three-dimensional Lippmann-Schwinger, and PW represents partial wave. Non-relativistic results are denoted (NR) and relativistic results are denoted (REL).

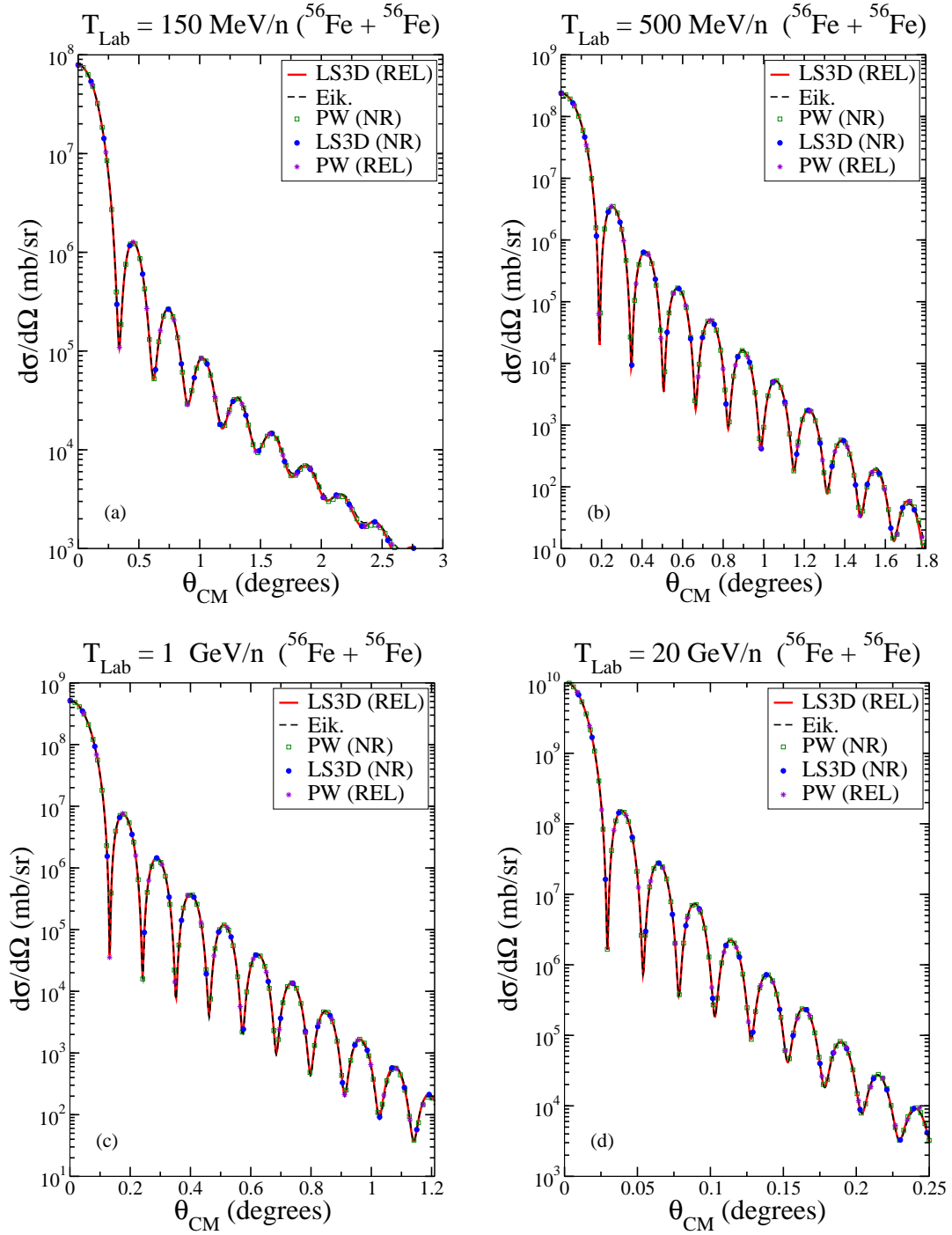


Figure 24: Elastic differential cross sections for $^{56}\text{Fe} + ^{56}\text{Fe}$ reactions for projectile lab kinetic energies of 150, 500, 1000, 20000 MeV/n. Eik. represents eikonal, LS3D represents three-dimensional Lippmann-Schwinger, and PW represents partial wave. Non-relativistic results are denoted (NR) and relativistic results are denoted (REL).

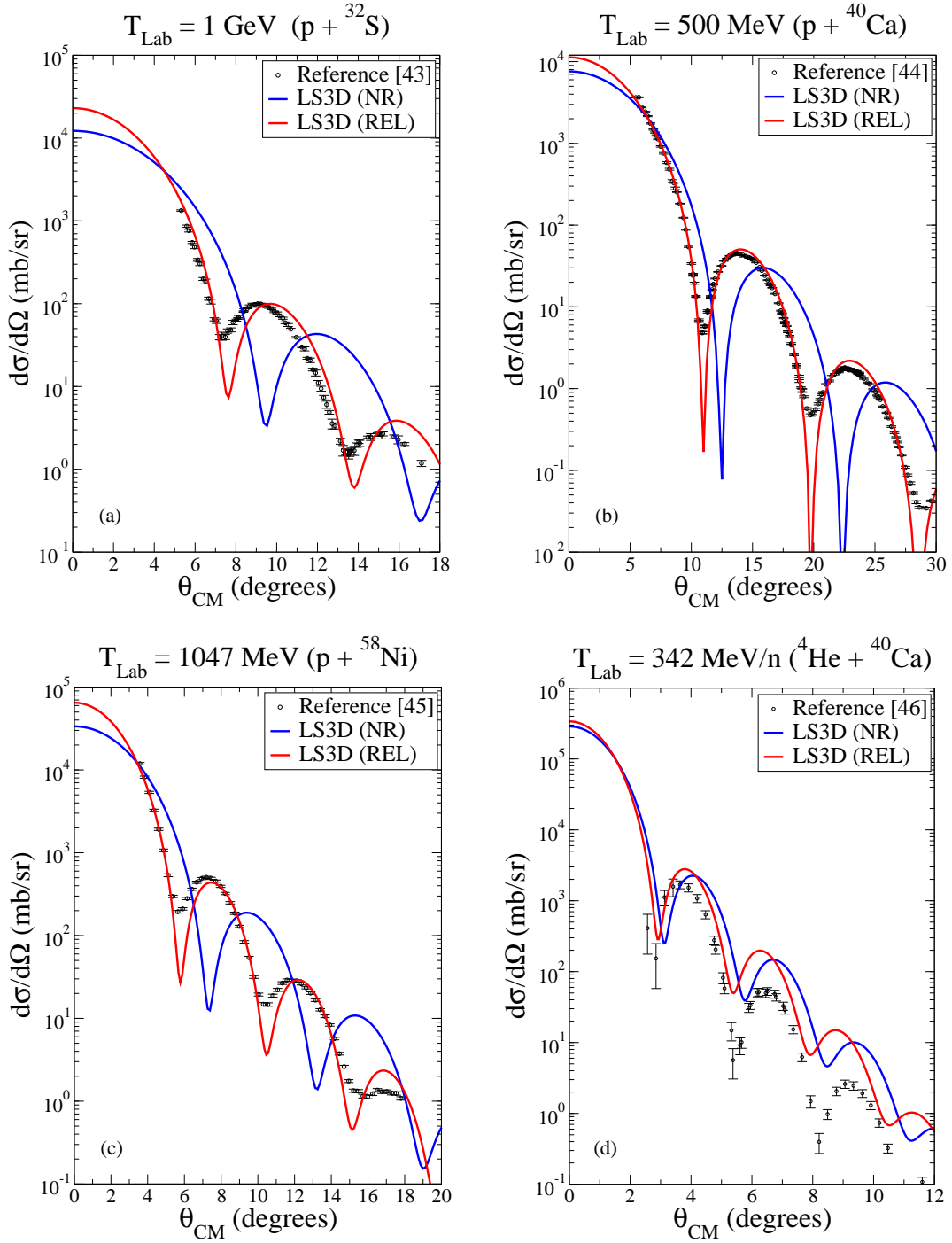


Figure 25: Elastic differential cross sections for (a) $p + {}^{32}\text{S}$ at $T_{Lab} = 1 \text{ GeV}$ [43] (b) $p + {}^{40}\text{Ca}$ at $T_{Lab} = 500 \text{ MeV}$ [44] (c) $p + {}^{58}\text{Ni}$ at $T_{Lab} = 1 \text{ GeV}$ [45] and (d) ${}^4\text{He} + {}^{40}\text{Ca}$ at $T_{Lab} = 347 \text{ MeV/n}$ [46].

REPORT DOCUMENTATION PAGE					Form Approved OMB No. 0704-0188	
<p>The public reporting burden for this collection of information is estimated to average 1 hour per response, including the time for reviewing instructions, searching existing data sources, gathering and maintaining the data needed, and completing and reviewing the collection of information. Send comments regarding this burden estimate or any other aspect of this collection of information, including suggestions for reducing this burden, to Department of Defense, Washington Headquarters Services, Directorate for Information Operations and Reports (0704-0188), 1215 Jefferson Davis Highway, Suite 1204, Arlington, VA 22202-4302. Respondents should be aware that notwithstanding any other provision of law, no person shall be subject to any penalty for failing to comply with a collection of information if it does not display a currently valid OMB control number.</p> <p>PLEASE DO NOT RETURN YOUR FORM TO THE ABOVE ADDRESS.</p>						
1. REPORT DATE (DD-MM-YYYY)		2. REPORT TYPE			3. DATES COVERED (From - To)	
01-09 - 2014		Technical Publication				
4. TITLE AND SUBTITLE Elastic Differential Cross Sections				5a. CONTRACT NUMBER		
				5b. GRANT NUMBER		
				5c. PROGRAM ELEMENT NUMBER		
6. AUTHOR(S) Werneth, Charles M.; Maung, Khin M.; Ford, William P.; Norbury, John W.; Vera, Michael D.				5d. PROJECT NUMBER		
				5e. TASK NUMBER		
				5f. WORK UNIT NUMBER 651549.02.07.01		
7. PERFORMING ORGANIZATION NAME(S) AND ADDRESS(ES) NASA Langley Research Center Hampton, VA 23681-2199				8. PERFORMING ORGANIZATION REPORT NUMBER L-20452		
9. SPONSORING/MONITORING AGENCY NAME(S) AND ADDRESS(ES) National Aeronautics and Space Administration Washington, DC 20546-0001				10. SPONSOR/MONITOR'S ACRONYM(S) NASA		
				11. SPONSOR/MONITOR'S REPORT NUMBER(S) NASA/TP-2014-218529		
12. DISTRIBUTION/AVAILABILITY STATEMENT Unclassified - Unlimited Subject Category 93 Availability: NASA CASI (443) 757-5802						
13. SUPPLEMENTARY NOTES						
14. ABSTRACT The eikonal, partial wave (PW) Lippmann-Schwinger, and three-dimensional Lippmann-Schwinger (LS3D) methods are compared for nuclear reactions that are relevant for space radiation applications. Numerical convergence of the eikonal method is readily achieved when exact formulas of the optical potential are used for light nuclei ($A \leq 16$) and the momentum-space optical potential is used for heavier nuclei. The PW solution method is known to be numerically unstable for systems that require a large number of partial waves, and, as a result, the LS3D method is employed. The effect of relativistic kinematics is studied with the PW and LS3D methods and is compared to eikonal results. It is recommended that the LS3D method be used for high energy nucleon-nucleus reactions and nucleus-nucleus reactions at all energies because of its rapid numerical convergence and stability.						
15. SUBJECT TERMS Elastic differential Cross section; Relativistic kinematics						
16. SECURITY CLASSIFICATION OF:			17. LIMITATION OF ABSTRACT	18. NUMBER OF PAGES	19a. NAME OF RESPONSIBLE PERSON	
a. REPORT	b. ABSTRACT	c. THIS PAGE			STI Help Desk (email: help@sti.nasa.gov)	
U	U	U	UU	64	19b. TELEPHONE NUMBER (Include area code) (443) 757-5802	